Ph.D Thesis

Search for solar Kaluza-Klein axion by annual modulation with the XMASS-I detector

OKA Naoya

Department of Physics, Graduate School of Science,
Kobe University

July, 2017

Abstract

Hypothetical particle axion is introduced to solve the strong CP problem. In theories of the large extra dimensions, which are introduced to solve the gauge hierarchy problem, axions could propagate in the extra dimensions beyond the standard 4-dimensional spacetime, and would acquire Kaluza-Klein (KK) excitations, which could be observed as particles with heavier masses in the standard spacetime. These KK axions possibly be produced in the Sun are thought to solve unexplained heating of the solar corona. A small fraction of the solar KK axions would have velocities less than the solar escape velocity and be trapped in the solar system. They would decay into two photons inside the terrestrial detector. In this study, the decay of the solar KK axions was searched using 832×359 kg·days of XMASS-I data by the annual modulation analysis. No significant excess over expected background is found, and the first experimental constraint on KK axion-photon coupling of $4.8 \times 10^{-12} \, \mathrm{GeV}^{-1}$ for KK axion number density $\bar{n}_{\mathrm{a}} = 4.07 \times 10^{13} \, \mathrm{m}^{-3}$ (90% CL) is set.

Acknowledgements

iv

Contents

1

Introduction

1.1 Overview

In this section, the current status of particle physics and two problems therein closely related to this thesis are summarized.

1.1.1 The standard model of elementary particles

Particle physics is an attempt to explain what comprises the Universe and what are the forces among them. By 1970s, the Standard Model (SM) of the particle physics was formulated [1], and it was finally confirmed by the discovery of Higgs boson in 2012 [2, 3]. Elementary particles in SM are shown in Table 1.1. SM describes the properties of the particles, the mass, the charge, the spin, how they interact, etc. In SM, there are four kinds of forces: the elecro-magnetic interaction, the weak interacion, the strong interacion and the gravitational interaction. Although predictions by SM are widely consistent with results from various experiments, there still remain some questions we do not have the answer. Therefore, physics beyond the SM is thought to be necessary to solve these problems. The subject of this thesis is related to two of these problems.

Table 1.1: Elementary particles in the standard model.

quarks	u	c	t
	d	s	b
leptons	e	μ	τ
	ν_e	ν_μ	ν_τ

gauge bosons	γ	W, Z	g
Higgs		H	

1.1.2   Problem 1: The strong CP problem

Why does our Universe consist of matter, not antimatter? The answer to explain this question is the Baryon asymmetry in the early Universe. This scenario starts with an asymmetry that the baryon number is slightly larger than the anti-baryon number. After the baryon and anti-baron pair annihilation, there remained small number of baryons, which formed the Universe. This asymmetry can arise from the violation of CP symmetry in the weak interaction [4]. The CP violation in the weak interaction was observed, which is well-explained by the SM. The SM also predicts the CP violation in the strong interaction, but it has not been observed by any experiment yet. This is not explained by SM and it is known as the strong CP problem. A hypothetical particle called axion could be the key to solve the problem. We will discuss the problem in Chapter 2.

1.1.3   Problem 2: The gauge hierarchy problem

The gravitational force is the most familiar force to the human being on the Earth. Everyone on the Earth is living in the Earth's gravity. However, in microscopic view, the gravity is extremely weak compared to other three kinds of forces. The reason for this many orders of magnitude difference is not known and the mystery is called the gauge hierarchy problem. In Chapter 3 we will introduce elegant ideas to solve the problem, the theories of extra dimensions. These theories introduce one or more extra dimensions to our standard 3 (space) + 1 (time) dimensions' universe. In the extra dimension theories, motions of particles in extra dimensions would be observed as new particles in our 4-dimensional spacetime, which are called Kaluza-Klein (KK) particles. Existence of such KK particles could be a strong evidence of extra dimensions.

1.1.4   The target: Kaluza-Klein axion

Axions and extra dimensions can solve the problems of SM as mentioned above. Then, if axions exist and propagate in extra dimensions, there should exist KK axions, and we may have a chance to detect them. The goal of this study is to search for KK axions produced in the Sun. For that, XMASS-I, a large liquid xenon detector located at 1000 m underground was used.

1.2   Outline of this thesis

This thesis is composed of 8 chapters. In the first four chapters, theoretical background and the motivation are discussed. In chapter 1, we saw two problems in the standard model of particle physics, the strong CP problems and the gauge

hierarchy problems. Kaluza-Klein axion, the subject of this thesis, is closely related to these two problems. Chapter 2 covers how to solve the first question by introducing a particle called axion. In Chapter 3 we explore the theory of extra dimensions, a possible solution to the second question. Then, in Chapter 4, we review the preceding studies on KK axion.

Chapters 5 to 7 are concerned with the experimental observation and analysis. Chapter 5 explains the XMASS-I detector used for this study. In chapter 6 we discuss the analysis methods and results on the KK axion search. The results are discussed in Chapter 7. Finally, Chapter 8 provides a conclusion.

2

The strong CP problem and Axions

"It surrounds us and penetrates us. It binds the galaxy together."
    – Obi-Wan Kenobi, *STAR WARS Episode IV A NEW HOPE*

2.1 The strong CP problem

The strong interaction, which confines quarks and gluons as a hadron, is described by the quantum chromodynamics (QCD). The general form of Lagrangian of QCD includes following term:

$$\mathcal{L}_\theta = \bar{\theta}\frac{g_s^2}{32\pi^2}G_{\mu\nu}^a\tilde{G}^{a\mu\nu}. \qquad (2.1)$$

Here, $G_{\mu\nu}^a$ is the QCD field strength, and g_s is the coupling constant of strong interaction. $\bar{\theta}$ is defined by

$$\bar{\theta} = \theta + \arg\det M_q. \qquad (2.2)$$

θ is called the strong-interaction θ-angle or θ vacuum, and M_q is the Cabibbo-Kobayashi-Maskawa (CKM) matrix. The term $\mathcal{L}_\theta$ is CP-violating unless $\bar{\theta}$ is zero. Experimentally, $\bar{\theta}$ can be known by measuring the electric dipole moment of neutron (nEDM). Experimental result shows [5]:

$$d_n < 3.0 \times 10^{-26}e \cdot \text{cm} \ (90\% \ \text{C.L.}). \qquad (2.3)$$

Meanwhile, theoretically expected value of nEDM $d_n(\bar{\theta})$ is [6] :

$$d_n(\bar{\theta}) \sim \bar{\theta} \cdot \left(6 \times 10^{-17}\right) e \cdot \text{cm}. \qquad (2.4)$$

4

From Equation (2.4) and (2.3), $\bar{\theta}$ can be evaluated as

$$\bar{\theta} < 10^{-10}. \tag{2.5}$$

To realize such a small value of $\bar{\theta}$, the phase of quark mass matrix M_q in Equation (2.2) needs to be fine-tuned with θ at a precision of 10^{-10}. This fine-tuning problem is called the strong CP problem.

2.2 Introduction of axions

As described in [7], R. D. Peccei and H. Quinn introduced a global quasi-symmetry $U_{\mathrm{PQ}}(1)$ in order to solve the strong CP problem. The axion is a pseudo-Nambu-Goldstone boson which emerges when $U_{\mathrm{PQ}}(1)$ spontaneously breaks down.
By introducing the axion field $a(x)$, Equation (2.1) becomes:

$$\mathcal{L}_\theta = \left(\bar{\theta} - \frac{a(x)}{f_{\mathrm{a}}} \right) \frac{g_s^2}{32\pi^2} G_{\mu\nu}^a \tilde{G}^{a\mu\nu}. \tag{2.6}$$

where f_{a} denotes the energy scale of the axion and is called the axion decay constant. Because the axion potential $V(\bar{\theta})$ is minimum when $\bar{\theta} = a(x)/f_{\mathrm{a}}$, the CP-violationg term of the QCD Lagrangian vanishes and the strong CP problem is solved. Immediately after the introduction of PQ symmetry, S. Weinberg [8], F. Wilczek [9], W. A. Bardeen and S. H. H. Tye [10] studied properties of the axion. This model was called PQWW model. The axion mass is expressed by:

$$m_{\mathrm{a}} = \frac{\sqrt{Z}}{1+Z} \frac{f_\pi m_\pi}{f_{\mathrm{a}}} \approx 6 \times 10^{-6} \, \mathrm{eV} \left(\frac{10^{12} \, \mathrm{GeV}}{f_{\mathrm{a}}} \right), \tag{2.7}$$

where $Z = m_u/m_d$. m_π and f_π are the mass and the decay constant of the neutral pion [10]. Since f_{a} was considered to be close to electro-weak scale (~ 100 GeV) in PQWW model, m_{a} is calculated to be ~ 100 keV. However, such particle was not discovered.

2.3 Invisible axions

After PQWW axion was excluded, two models of "invisible" axion with larger f_{a} were proposed. One is called DFSZ model[11, 12], and the other is called KSVZ model[13, 14] or hadronic axion since it does not couple with lepton in the tree level. For both models, mass of the invisible axion is represented by Equation (2.7). The model-dependent axion-photon coupling constant is denoted as:

$$g_{\mathrm{a}\gamma\gamma} = \frac{\alpha}{2\pi f_{\mathrm{a}}} \left(\frac{E}{N} - \frac{2}{3} \frac{4+Z}{1+Z} \right). \tag{2.8}$$

Here, α is the fine structure constant, and for DFSZ, $E/N = 8/3$ and for KSVZ, $E/N = 0$. One example of axions' coupling with two photons is Primakoff effect. Photons are converted to axions in a strong electromagnetic field. The Feynman diagrams of Primakoff effect and its inverse process are shown in Figure 2.1. In these diagrams, one of the photons is a real photon and the other is the electromagnetic field which acts as a virtual photon. Axions are considered to be produeced by Primakoff effect in stars which have strong electromagnetic field.
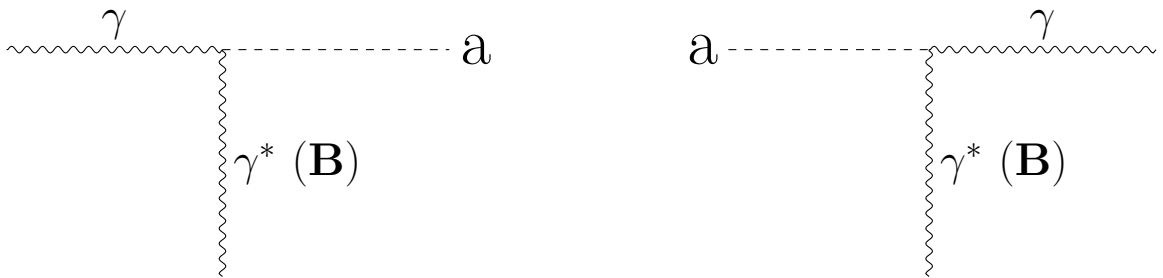
Figure 2.1: The Feynman diagram of Primakoff effect (left) and inverse Primakoff effect (right) of axions. In both diagrams, a represents an axion, γ shows a photon, and γ^* is the virtual photons representing the magnetic field **B**. Diagrams in this thesis is made with Tikz-Feynman [15].

Also, axions can be produced from two photons via photon coalescence and can decay into two photons. The photon coalescence process is shown in Figure 2.2.
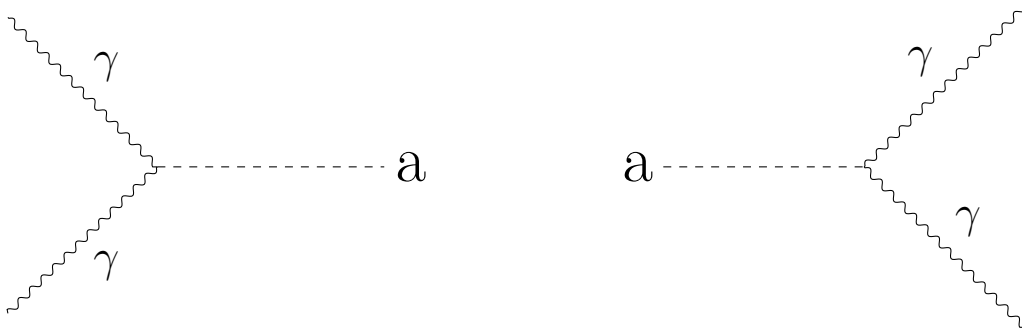
Figure 2.2: The Feynman diagram of photon coalescence (left) and axion's decay (right).
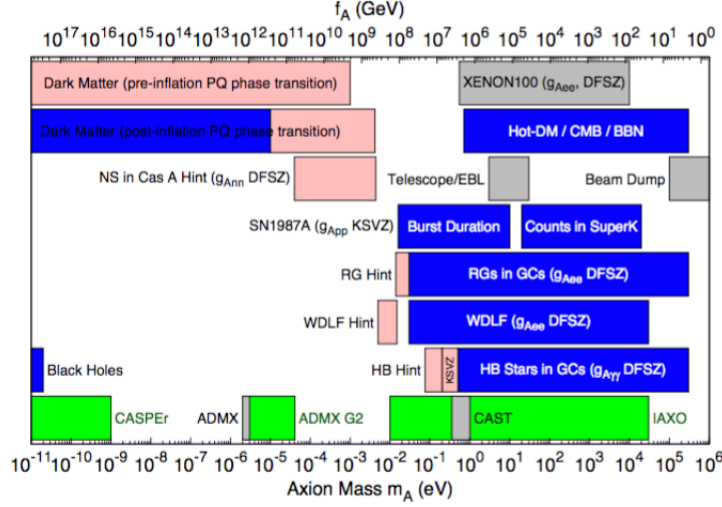
Figure 2.3: Exclusion limits and hints on the axion by various measurements and calculations. The horizontal axis is the axion mass or f_a. Blue bands shows the excluded range by cosmological and astrophysical observations. Gray ranges show the exclusion by experiments and green ones are projected reach. Light red boxes indicate the hints from various observations (NOT exclusions). Taken from the review by Particle Data Group [16].

2.4 Current constraints for axion

There have been many observations and experiments to search for the invisible axions. The axion has not been detected so far, and obtained limits are summarized in Figure 2.3. Some explanations and interpretations of Figure 2.3 are listed below.

- 'Dark matter' in Figure 2.3 shows the regions that axion can be the dark matter in Universe. Axions are produced by PQ phase transition in the early Universe. If the transition is after the inflation, the blue range is excluded.

- 'XENON100' shows the limit from the measurement of axio-electric effect which is explained in Section 2.5.2.

- 'HB stars in GCs' means horizontal branch stars in globular-cluster. If axion-photon coupling $g_{a\gamma\gamma}$ is large, more energy is taken away by axions produced in HB stars, and the evolution goes faster and the number of observable HB stars would be less than we observe. Thus we can set the limit on f_a using Equation (2.8).

- In the bottom row, limits by direct search experiments ADMX [17] and CAST [18] are shown in the gray bands. The reaches of future experiments

CASPEr [19], and IAXO [20] are shown in the green bands. See Section 2.5 for detail on the direct detection.

In summary, the open window for the axion decay constant is [1]:

$$10^{10} \, \text{GeV} < f_\text{a} < 10^{12} \, \text{GeV}. \tag{2.9}$$

This can be converted to the mass bound using Equation (2.7):

$$10^{-5} \, \text{eV} < m_\text{a} < 10^{-3} \, \text{eV}. \tag{2.10}$$

2.5   Axion searches

P. Sikivie proposed two methods to detect invisible axions called, namely, axion haloscope and axion helioscope [21, 22]. Both experiments are based on the effect of the axion's coupling with two photons. To date, many other methods using other interactions have been proposed. A few examples are explained in the following subsections.

2.5.1   Axion-photon coupling

Axion haloscope

Cold axions produced in the early universe would exist in our galaxy in the form of the galactic halo, or the dark matter. To detect them on the Earth, we can use an apparatus called "microwave cavity". The schematic explanation of the axion haloscope is shown in Figure 2.4. In the cavity, axions would interact with virtual photons (γ^*) of the strong magnetic field (B) and would be converted into photons (γ) with the wavelength of the microwave region. If that wavelength matches with the frequency of the cavity, we should observe a resonance. The axion mass can be scanned by tuning the cavity's frequency. ADMX [17] and the experiment at Yale University [23] are two of the currently running axion haloscope experiments. Currently, halo scope experiments rule out $g_{\text{a}\gamma\gamma}$ above $10^{-13} \, \text{GeV}^{-1}$ for m_a between $10^{-5} - 10^{-6}$ eV as shown in Figure 2.7.

Axion helioscope

Axions can be produced by the Primakoff effect from photons and strong magnetic fileds in the Sun. These axions are called solar axions and a part of these solar

---

[1]The upper bound for f_a in Equation (2.9) (or the lower bound for m_a in Equation (2.10)) comes from the assumtion that the PQ phase transition occurred after the inflation. If the transition occurred before the inflation, this bound is no more valid.
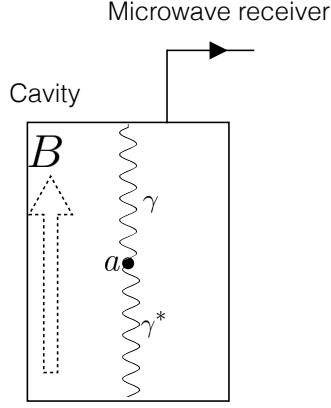
Figure 2.4: Schematic view of the haloscope experiments. B, a, γ, and γ^* respectively represent the magnetic field, a dark matter halo axion, a microwave photon converted from axion, and a virtual photon.

axions radiate from the Sun and reach the Earth. By applying strong magnetic fields in the laboratory, these axions would in turn be converted into photons through the inverse Primakoff process. Since the temperature of the core of the Sun is about 10^7 K, observed photons have energy of $\sim$ keV. By detecting these X-rays we can observe solar axions. Tokyo axion helioscope (Sumico) [24], CAST [18] and IAXO [20] are the axion helioscope experiments. Currently, constraint from helioscope experiments is $g_{a\gamma\gamma} < 10^{-10}$ GeV^{-1}. Around $m_a \sim 1$ eV, they exclude KSVZ model.

LSW experiment

Axions can be generated and detected in a laboratory and this approach is used in such experiments called Light-Shining-Though-Wall (LSW) experiments [25, 26, 27, 28, 29]. In these experiments, high-intensity laser is injected toward the wall in front of the photon detector. In both spaces optically separated by the wall, there are strong magnetic fields which causes photon-axion conversion and axion-photon conversion. Axions converted from the photons in the first magnetic field can go through the wall because of its invisible nature, and can be converted into photons in the second magnetic field. The detector waits for the signal of those photons.
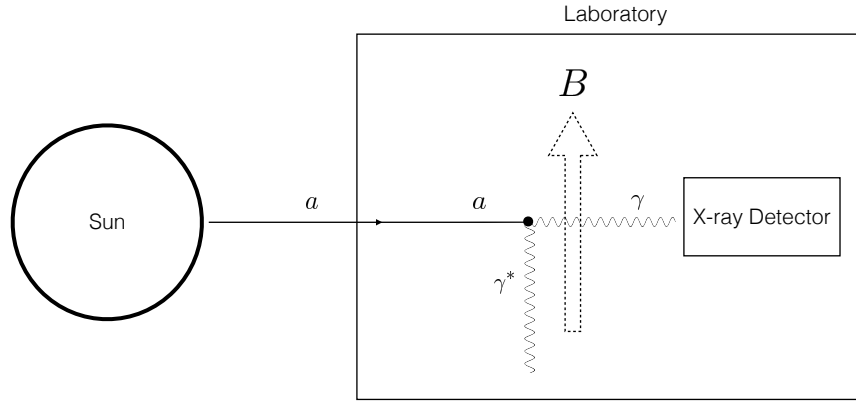
Figure 2.5: Schematic view of the helioscope experiments. B, a, γ, and γ^* represent the magnetic field, a solar axion, an X-ray photon converted from axion, and a virtual photon, respectively. The axion produced in the Sun reach the laboratory on the Earth, where it interacts with a virtual photon and is converted into an X-ray photon.
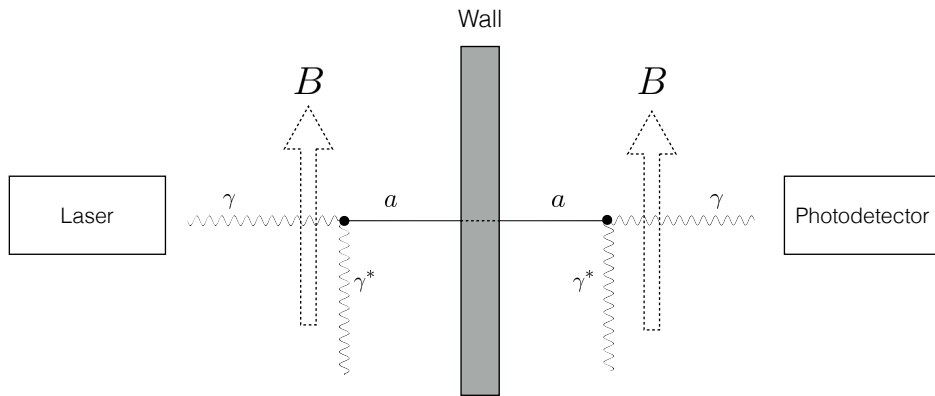
Figure 2.6: Schematic view of LSW experiments.
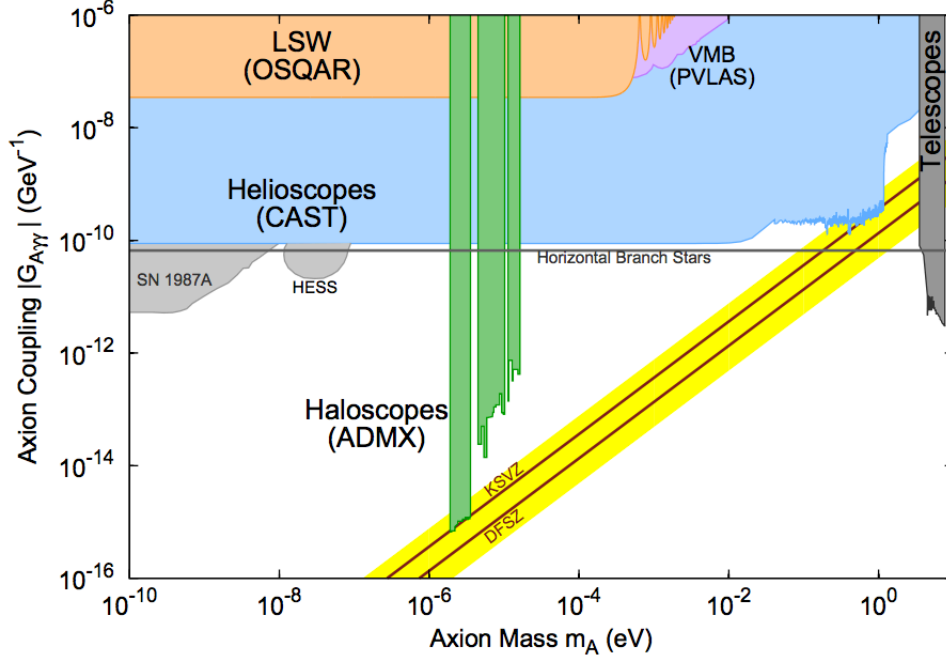
Figure 2.7: Current status of axion searches using the axion-photon coupling.(from the review by Particle Data Group [16])

Status of axion-photon coupling search

Figure 2.7 shows the current status of the axion searches using the axion-photon couplings. In this figure, the yellow band shows the region of prediction by KSVZ and DFSZ model. Helioscope experiment (CAST) and Haloscope experiment (ADMX) touch the band around 1 eV and 1 μ eV respectively, but axions have not yet been discovered. Since many new experiments are proposed, axions may be captured in the near future [30, 31, 32, 33, 34, 35].

2.5.2 Axion-electron coupling

Axion-electron coupling is also used for the axion search. Solar axions produced by the Compton-like scattering of photons on electrons and the bremsstrahlung from electrons are searched by terrestrial detectors. In the detector side, these solar axion can cause reaction similar to the photo-electic effect, which is called axio-electric effect [36]. The signal is about keV, and can be effectively searched by direct WIMP dark matter detectors. Expected signal spectra of axio-electic effect of solar axions for germanium, argon, and xenon detectors are shown in Figure 2.8. XMASS [37] and other experiments such as Russian group [38], EDELWEISS-
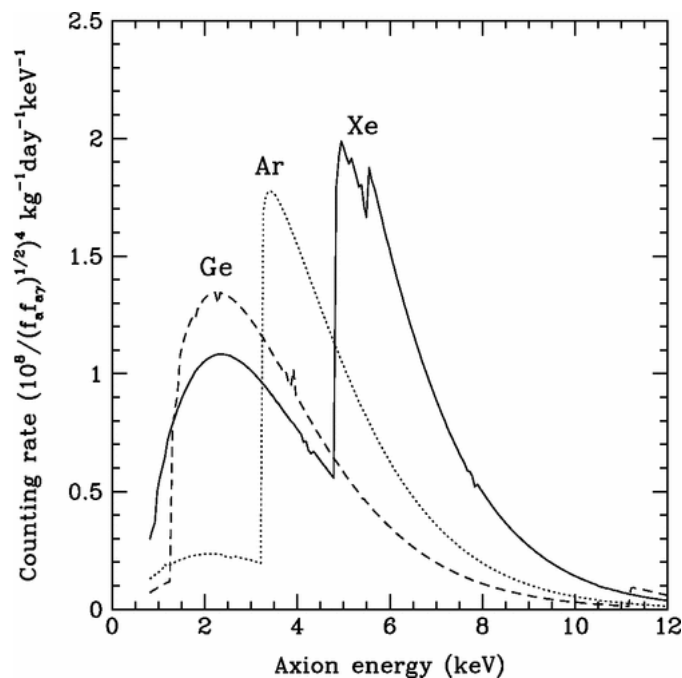
Figure 2.8: Expected signal spectra of axio-electic effect of solar axions for germanium, argon, and xenon detectors. Taken from [36].

II[39], XENON100 [40], and KIMS [41] have searched solar axions using this effect. Figure 2.9 shows the limit on the axion-electron coupling.

2.5.3　Axion-nucleon coupling

Axion-nucleon interaction can be used for the axion search [42]. ^{57}Fe in the Sun can be excited and its de-excitation can emit monochromatic axion (14.4 keV). These axions from the Sun can excite ^{57}Fe in a laboratory, and we can detect a photon with 14.4 keV emitted when the nucleus relaxes to the ground state. Recently, this type of search is performed using 9.4 keV of ^{83}Kr [43]. The constraint from this experiment is $m_a < 100$ eV (95% CL).
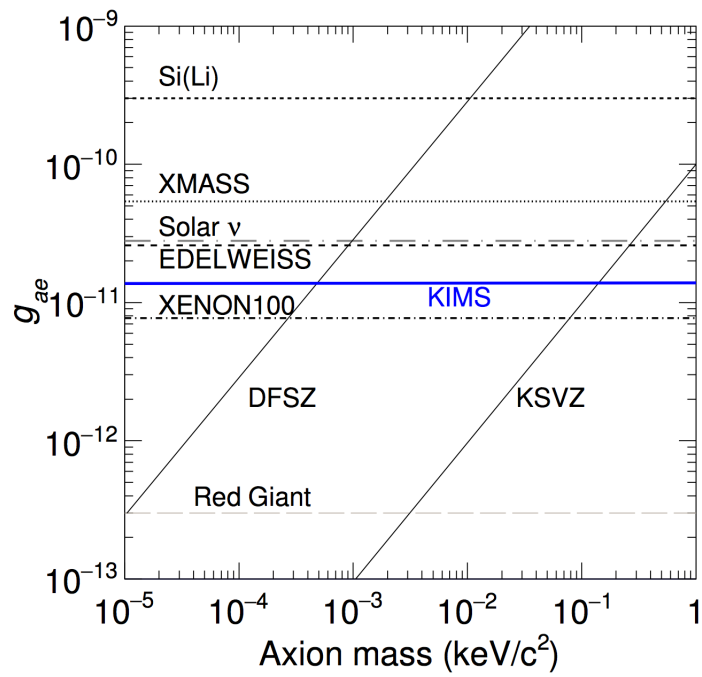
Figure 2.9: Limit on axion-electon coupling. Taken from [41]. The area above each line is rejected by corresponding experiment or astrophysical observation.

3

The gauge hierarchy problem and theories of extra dimensions

"L'essential est invisible pour les yeux."

– Antoine de Saint-Exupéry, *Le Petit Prince*

3.1   The gauge hierarchy problem

The gauge hierarchy problem is the problem that why the gravitational force is extremely weak compared to the other kinds of forces in the microscopic scale. Table 3.1 shows the difference between the electro-weak scale and the Planck scale.

Table 3.1: The electro-weak scale and the Planck scale

electro-weak scale	$M_{\mathrm{EW}} = 1/\sqrt{G_{\mathrm{F}}} \sim 100\,\mathrm{GeV}$
Planck scale	$M_{\mathrm{Pl}} = 1/\sqrt{G} \sim 10^{19}\,\mathrm{GeV}$

Here, G_{F} is Fermi coupling constant, G is gravitational coupling constant [1]. The difference between the Planck scale and the electro-weak scale is so large $\sim 10^{17}$, and this mystery is called the gauge hierarchy problem.

---

[1]Some difference exists in the definition of Planck scale depending on using Newtons's constant G or Einstein's constant $\kappa = \frac{8\pi G}{c^4}$.

14

3.2 Kaluza-Klein theory

3.2.1 Introduction of Kaluza-Klein theory

Theories of extra dimensions claim the existence of higher dimensions in addition to the standard (3+1) spacetime. One of these theories was first developed by Kaluza [44] and sophisticated by Klein [45], and is now called the "Kaluza-Klein theory". Their motivation was the unification of the gravitational force and the electromagnetic force. Their trial did not succeed, but the idea has been attractive. Especially, at the end of the last century, theories of the extra dimensions became popular because it was shown that new theories of the extra dimensions have a possibility to solve the gauge hierarchy problem. In this chapter, these relatively new theories will be reviewed.

3.2.2 Kaluza-Klein mode

One possible clue of the existence of the extra dimensions is called "Kaluza-Klein (KK) mode". Extra dimensions are thought to be "compactified" in a certain radius R. Motions of a particle in the extra dimensions can be seen as mass states or "KK excitations" which are separated in $1/R$. Those states are also called "KK particles". The mass states of KK particles are written as

$$m_n = \frac{n}{R} \ (n = 1, ..., \infty), \tag{3.1}$$

where m_n is the mass of the n-th KK mode, and R is the compact radius as illustrated in Figure 3.1. Since infinite number of mass states exist, they are also called "KK tower". Since compact radius R had been believed to be as small as Planck scale ($\approx 10^{-34}$ m), even the lightest KK mode seemed not experimentally detectable because its mass would be $1/R \approx 10^{18}$ GeV. However, a new theory with detectable extra dimensions emerged in 1998, making the extra dimensions a hot topic.
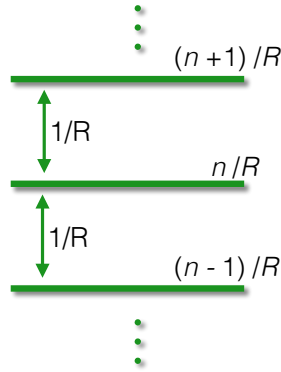
Figure 3.1: The KK tower. The n-th KK mode has mass of n/R, as denoted in Equation (3.1).

3.3   Large extra dimensions

3.3.1   Introduction of large extra dimensions

N. Arkani-Hamed, S. Dimopoulos, and G. Dvali introduced a scenario with ~mm scale extra dimensions to solve the gauge hierarchy problem [46, 47, 48]. Their model is called the "ADD model" or the "large extra dimensions" (LED), because ~mm scale extra dimensions were far larger than people had been imagined. It may be also called the model with "flat" extra dimensions, in contrast to the model with "warped" extra dimensions which will be mentioned in Section 3.4.

In theories of large extra dimensions, our 3-dimensional space is considered as a brane in a higher-dimensional bulk (brane world scenario). While electro-magnetic, weak, and strong interactions are confined within the brane, only gravity can propagate in the bulk. Then the hierarchy problem can be solved in the following way.

Extra dimensions are compactified in the compact radius R. In shorter distance than R ($r \ll R$), gravitational potential $V(r)$ between two masses m_1, m_2 is written as:

$$V(r) \approx \frac{m_1 m_2}{M_{\mathrm{F}}^{n+2}} \frac{1}{r^{n+1}} \quad (r \ll R). \tag{3.2}$$

Here, n is the number of extra dimensions, and fundamental scale M_{F} is the Planck scale in $(4+n)$-dimensional space. For $r \gg R$ this equation becomes:

$$V(r) \approx \frac{m_1 m_2}{M_{\mathrm{F}}^{n+2} R^n} \frac{1}{r} \quad (r \gg R). \tag{3.3}$$

Since this equation holds in macroscopic scale, it must be same as the gravitational potential in 4-dimensional spacetime:

$$V(r) \approx \frac{m_1 m_2}{M_{\mathrm{Pl}}^2} \frac{1}{r}. \tag{3.4}$$

From Equations (3.3) and (3.4), the following relation holds between M_{F} and M_{Pl}:

$$M_{\mathrm{Pl}}^2 \approx R^n M_{\mathrm{F}}^{n+2} \tag{3.5}$$

Now the Planck scale M_{Pl} is no longer fundamental, but is derived from the fundamental scale M_{F}. It is natural to expect M_{F} to be close to the electro-weak scale (~ 100 GeV). For example, by assuming $M_{\mathrm{F}} = 100$ TeV [2] in case of $n = 1$, R becomes

$$R \approx 10^{23} \text{ GeV}^{-1} \approx 10^7 \text{ m (for } n = 1, M_{\mathrm{F}} = 100 \text{ TeV)}. \tag{3.6}$$

With such a large value of R, we must observe a discrepancy from Newtonian gravity in the visible scale, so this case is immediately ruled out. For $n = 2$ case, R becomes:

$$R \approx 10^3 \text{ keV}^{-1} = 1 \text{ eV}^{-1} \approx 10^{-4} \text{ mm (for } n = 2, M_{\mathrm{F}} = 100 \text{ TeV)} \tag{3.7}$$

and it is allowed actually, because gravity in sub-milimeter scale has not been tested well.

One of the reasons this model is attractive is that the extra dimensions may exist in a detectable scale. We can test the model by measuring the gravity in the very short length with an experimental setup essentially same as Cavendish's experiment in 18th century [50]. Currently, 95% CL upper bounds on R are $R < 44$ μm for $n = 1$ and $R < 30$ μm for $n = 2$ [51].

3.3.2   Kaluza-Klein axions

Another interesting conclusion of TeV-scale LED is the existence of KK mode of a light particle with eV $-$ keV scale if it propagates through the bulk like the graviton can do. Let us consider the possibility that axions, like gravitons, propagate in the large extra dimensions. It is pointed out by the authors of ADD model [48] and others [52, 53, 54, 55] that we can make invisible axion without assuming large f_{a}. By assuming axions propagate in δ extra dimensions out of n, we would get a new axion decay constant:

$$\tilde{f}_{\mathrm{a}} \approx \left(\frac{M_{\mathrm{F}}}{M_{\mathrm{Pl}}} \right)^{\delta/n} f_{\mathrm{a}}. \tag{3.8}$$

---

[2]Since a cosmological bound $M_{\mathrm{F}} > 110$ TeV has been derived [49], we assume $M_{\mathrm{F}} = 100$ TeV here.

As we saw in Chapter 2, we have to assume a very large energy scale for invisible axions as in Equation (2.9). However, just like the gauge hierarchy problem, this produces another hierarchy problem. But now, extra dimensions can avoid this. If we assume $\delta = n = 2$ and $M_\mathrm{F} = 100$ TeV, we get 10^{-4} GeV $< \tilde{f}_\mathrm{a} < 10^{-2}$ GeV by using Equations (2.9) and (3.8).

Because f_a itself remains unchanged, properties of the axion are also same according to Equations (2.7) and (2.8). In addition, there would exist KK modes of axion as explained in Section 3.2.2. We call these KK modes as KK axion, and it is the subject of this study. We will see further on KK axion in Section 4.2.

3.4 Other models of extra dimensions

Besides LED, there are some attractive theories of extra dimensions. Although this study does not cover all of them, two models are introduced below.

Randall and Sundrum proposed a model called Randall-Sundrum model or "Warped extra dimensions" (WED) [56]. In WED, extra dimensions do not have to be compactified. We live in the weak brane (SM brane or TeV brane) and another brane called the gravity brane (Planck brane) exist. The weakness of the gravity in the weak brane is explained by the distance between our brane and the gravity brane in fifth dimension.

In the model of universal extra dimension (UED), all SM particles propagate in extra dimensions [57, 58]. The lightest Kaluza-Klein particle (LKP) with a mass at the TeV scale in UED scenario can be a candidate for the dark matter [59]. UED is different from above two brane-world scenarios (LED and WED) in the viewpoint that it will not solve the hierarchy problem.

4

Solar coronal heating problem and KK axions

In contrast to previous ones, this chapter covers a problem in the solar physics. In Section 4.1, we discuss so called the coronal heating problem of the Sun and some hypothetical candidates to solve it. Then in Section 4.2, we discuss another candidate, the solar KK axion, which is the subject of this thesis.

4.1 Coronal heating problem

Figure 4.1 shows the structure of the Sun. There is the core with temperature of 1.57×10^7 K inside the Sun. The optical surface of the Sun is called the photosphere. On the outside of the photosphere, there is a layer called the chromosphere, whose temperature is $\sim 10^4$ K. And the outside of the chromosphere is called the corona, which consists of ionized gas. Although the corona is outside of the surface, its temperature is two orders of magnitude higher ($\sim 10^6$ K) than that of the chromosphere. In Figure 4.2, we can see the temperature drastically rises in the transition region between the chromosphere and the corona. The mechanism causing this large difference has been unknown for over 70 years. This is called the coronal heating problem or the solar corona problem. Currently, two mechanisms are thought to be the most likely candidates to solve the problem: nanoflares and Alfvén waves.

4.1.1 Nanoflares

Solar flares are explosions occurring around the sunspots on the surface of the Sun, where strong magnetic field exists. Flares emit $10^{29} - 10^{33}$ erg of energy and are the most energetic events in the Sun. Although flares are so energetic that they
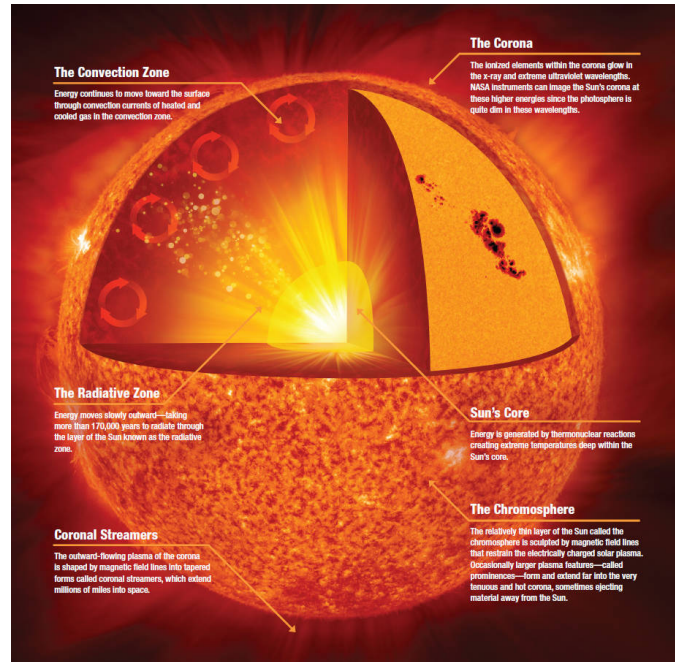
Figure 4.1: Structure of the Sun. Credit: NASA/Jenny Mottar. Taken from [60].
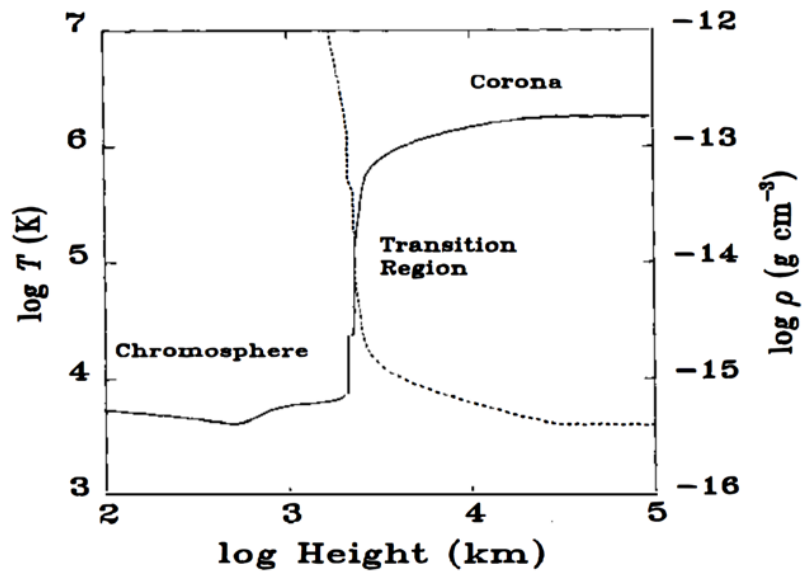
Figure 4.2: Temperature (solid line) and density (dashed line) of the solar chromosphere, the transition region, and the corona. Taken from [61].
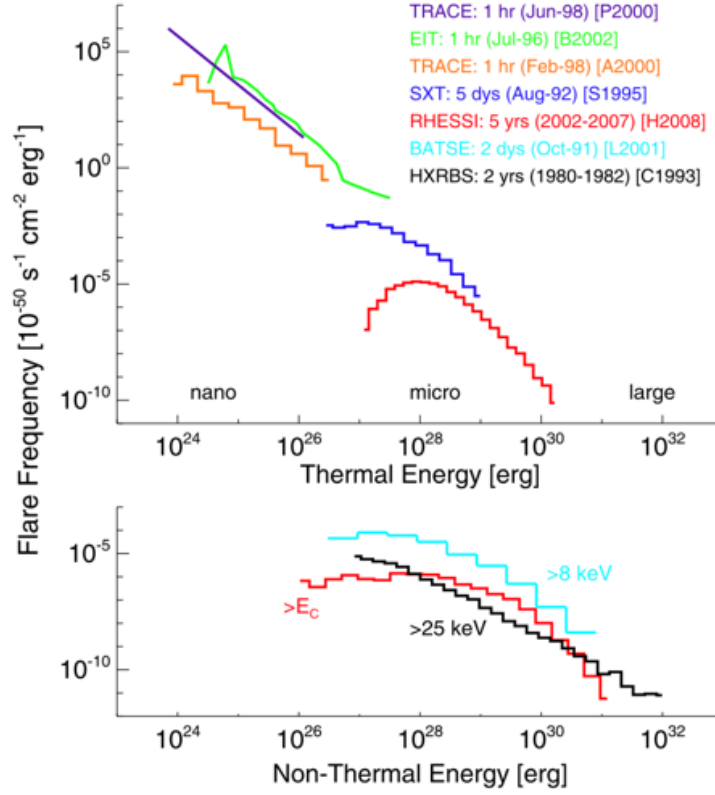
Figure 4.3: Energy distribution of solar flares. Taken from [66]. Each line shows different observation shown in the legend. The upper graph shows the observation of thermal radiations, and the lower graph shows the non-thermal observations.

sometimes affect the Earth, observed flares are not enough to explain the coronal heating. If there are flares which are too small to detect, they might explain the heating. Such flares are called nanoflares and have energy of $\sim 10^{24}$ erg [62]. After about 10 years from the prediction, nanoflares are observed by a solar observation satellite, *Hinode*[63, 64], and even picoflares are indicated [65]. Flares with smaller energy are more likely to occur as shown in Figure 4.3. However, even if we sum up the energy of these flares, it is still not enough for the heating. Searches for more faint flares are being continued.

4.1.2 Alfvén waves

Another candidate, Alfvén wave is a kind of magnetohydrodynamic (MHD) waves and is the oscillation of ions in a plasma [67]. If these waves transport and dissipate enough energy, corona can be heated. Figure 4.4 shows how MHD waves transport
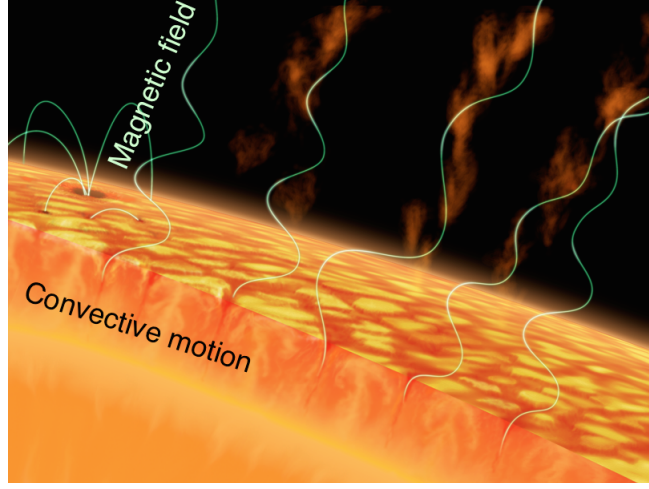
Figure 4.4: Schematic drawing of how MHD waves heating the corona. ©JAXA/NAOJ From [71]

energy. Alfvén waves have been observed in the Sun by *Hinode* satelite [68], and recently, by simultaneous measurement by *Hinode* and another solar observation satellite *IRIS*, dissipation of energy of Alfvèn wave through the process called resonant absorption was observed [69, 70]. Currently, only one event of dissipation has been observed and more events are needed to explain the coronal heating by Alfvén waves.

4.2   Solar KK axion

4.2.1   The solar KK axion model

Di Lella and Zioutas pointed out that KK axion can be a solution to the coronal heating problem [72, 73]. In their theory, KK axions interact with photons and thus are generated in the same manner as ordinary solar axions (by the Primakoff effect and the photon coalescence), and are emitted from the Sun. Since these thermally-produced solar KK axions have larger mass than that of ordinary axions due to the nature of the KK particles, a small fraction of them can be non-relativistic, and it can be trapped gravitationally by the Sun. To explain the X-ray emission from the Sun observed with an X-ray satellite, they assume the KK axion-photon coupling $g'_{a\gamma\gamma} = 9.2 \times 10^{-14}\,\mathrm{GeV}^{-1}$ as shown in Figure 4.5 [1] . KK axions around the Sun are accumulated since the beginning of the solar system. Current density

---

[1]In this thesis, we distinguish the ordinary axion-photon coupling $g_{a\gamma\gamma}$ from the KK axion-photon coupling $g'_{a\gamma\gamma}$.
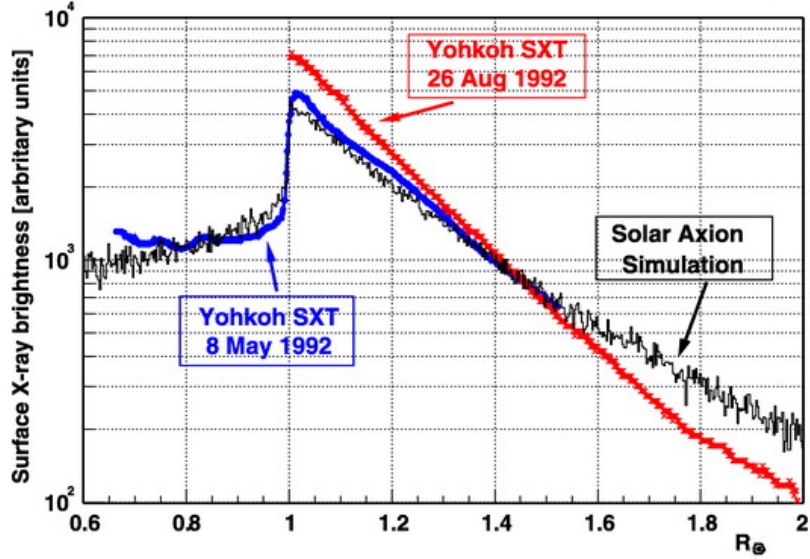
Figure 4.5: Soft X-ray flux distribution from the Sun in quiet periods by the observations of *Yohkoh* and by the simulation of solar KK axion. Taken from [73].

nearby the Earth is calculated by a simulation in [72] and is shown in Figure 4.6.

In the simulation, they assume the fundamental scale $M_F = 100$ TeV and the number of extra dimensions $n = 2$. Also, the number of extra dimensions that axions propagate is assumed as $\delta = 2$. From the value of M_F and n, the compact radius $R \sim 10^3 \, \text{keV}^{-1} = 1 \, \text{eV}^{-1}$ is derived. This leads to the separation of the each axion KK mode $(1/R)$ to be $1 \, \text{eV}$ from Equation (3.1).

The solar KK axions are produced by Primakoff effect and the photon coalescence. The energy spectra of these KK axions are shown in Figure 4.7. This figure shows that the fraction of massive KK axions produced by the photon coalescence is larger than that by Primakoff effect. Figure 4.8 shows the mass distribution of the trapped KK axions produced by each mechanism. By this reason, although the total flux of KK axion produced by the photon coalescence is smaller than that by Primakoff effect, the trapped density of KK axions by the photon coalescence is larger. Because the contribution of the Primakoff effect are 3 orders of magnitude lower, hereafter we will only discuss the contribution from the photon coalescence.

Trapped KK axions decay into 2 photons (a $\rightarrow \gamma\gamma$) with a lifetime of

$$t_a = \frac{64\pi}{g_{a\gamma\gamma}'^2 m_a^3} \tag{4.1}$$

where m_a is the mass of KK axions. These decay photons are typically in the
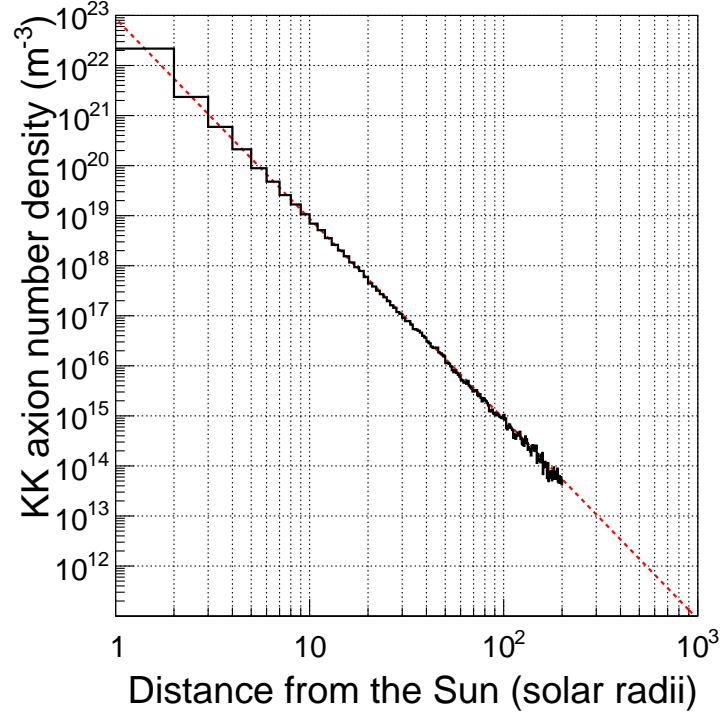
Figure 4.6: Number density of trapped KK axions against distance from the Sun. Black solid histogram shows the simulated distribution taken from [72] with $g'_{a\gamma\gamma} = 9.2 \times 10^{-14}\,\mathrm{GeV}^{-1}$. Red dotted line shows the fitted r^{-4} curve. The unit of distance is the radius of the Sun ($R_\odot = 695,700$ km). Using this unit, the distance between the Earth and the Sun is $211.4R_\odot$ at the perihelion and $218.6R_\odot$ at the aphelion, respectively.
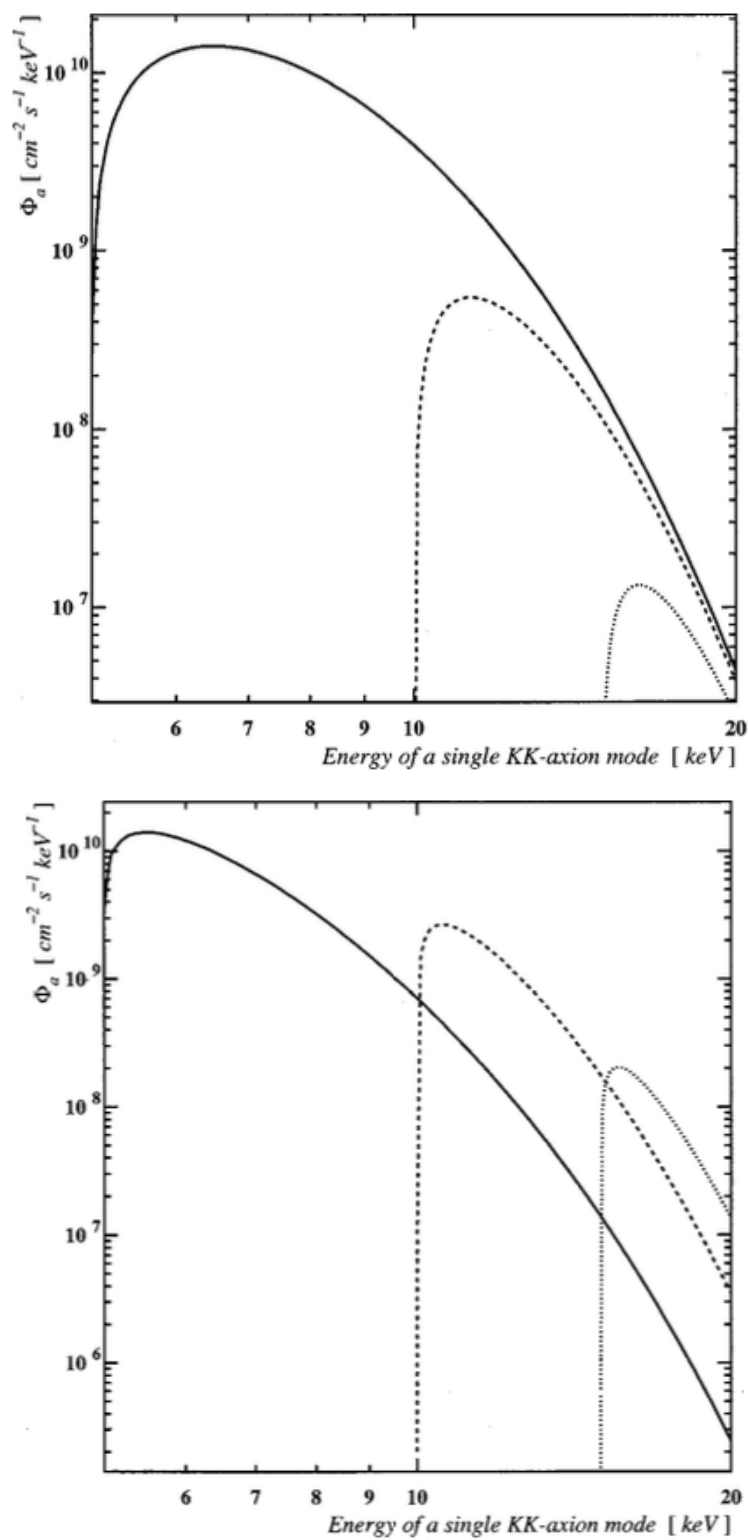
Figure 4.7: Energy dependence of the flux of solar KK axions at the position of the Earth. Taken from [54]. The upper graph shows that of due to Primakoff process, and the lower shows that of due to the Photon coalescence. Each line corresponds to the KK axion mode with $m_a = 5$ keV (solid), 10 keV (dashed), and 15 keV (dotted). Here, $g'_{a\gamma\gamma} = 10^{-10}\,\mathrm{GeV}^{-1}$ is assumed.
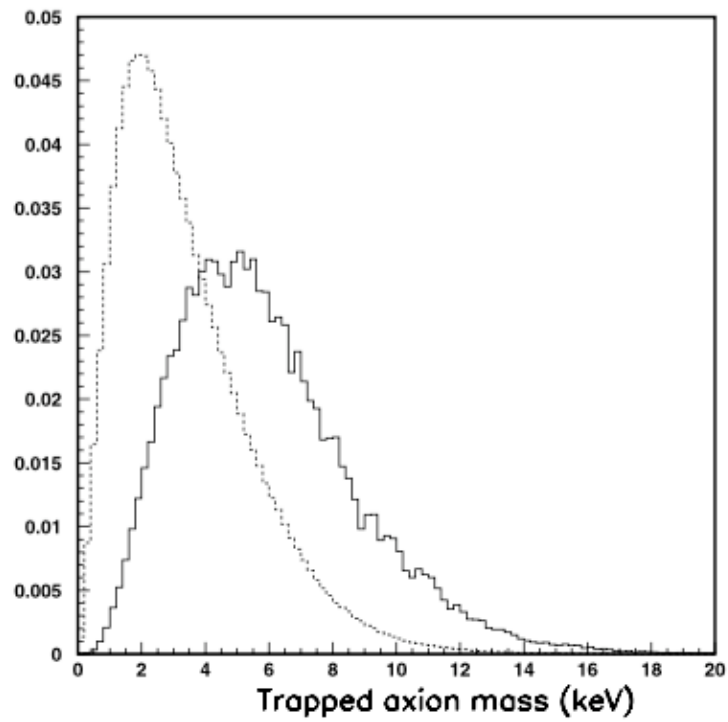
Figure 4.8: Mass distribution of gravitationally trapped solar KK axions. From [72]. Solid line shows those by photon coalescence and dotted line shows those by Primakoff effect. These spectra are normalized to unit area, so vertical axis has no absolute meaning.
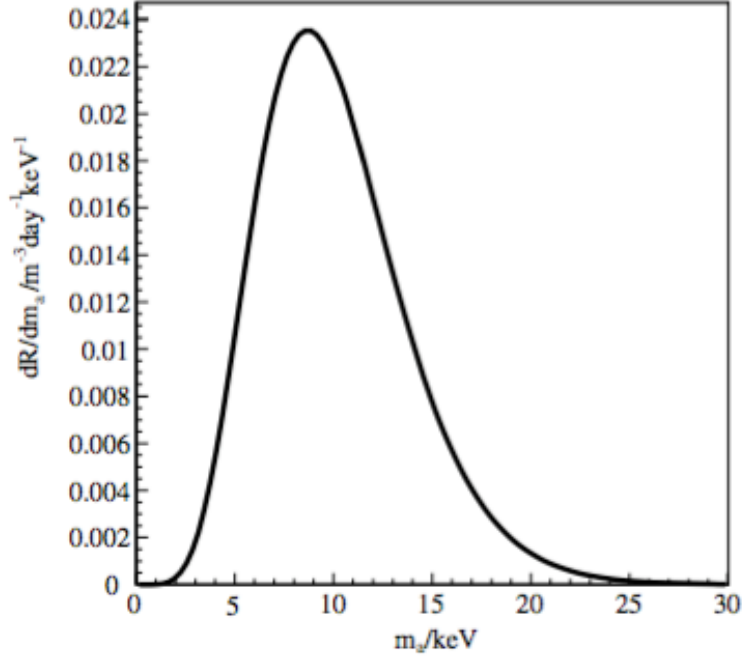
Figure 4.9: Decay spectra for trapped KK axions produced by photon coalescence. Here $g'_{a\gamma\gamma} = 9.2 \times 10^{-14}\,\text{GeV}^{-1}$ and local KK axion density of $\sim 10^{14}\,\text{m}^{-3}$ is assumed. From [74].

X-ray region by considering production rate, trapped rate (Figure 4.8) and decay rate for each KK axion mass. These X-ray may explain the coronal heating since the temperature of the corona ($\sim 10^6$ K) corresponds to the energy of X-rays.

4.2.2 KK axion search on the Earth

The density of KK axion around the Earth is calculated to be $\sim 10^{14}\,\text{m}^{-3}$ as shown in Figure 4.6. Gravitationally trapped KK axions are expected to decay in the terrestrial detector and the expected energy spectrum is shown in Figure 4.9. Here, $g'_{a\gamma\gamma} = 9.2 \times 10^{-14}\,\text{GeV}^{-1}$ and local KK axion number density of $\sim 10^{14}\,\text{m}^{-3}$ are assumed. From Figure 4.9, the expected KK axion decay rate R is denoted as

$$R = (2.5 \times 10^{11}\,\text{m}^{-3}\text{day}^{-1}) \left(\frac{g'_{a\gamma\gamma}}{\text{GeV}^{-1}}\right)^2 \left(\frac{n_a}{\text{m}^{-3}}\right). \tag{4.2}$$

Equation (4.2) is taken from Ref. [74]. The event rate at 10 keV is about $2 \times 10^{-2}\,\text{m}^{-3}\text{day}^{-1}\text{keV}^{-1}$, which is in reachable level with modern low-background detectors developed for dark matters. KK axion search is proposed by experiments using gas time projection chamber (TPC) such as an experiment using
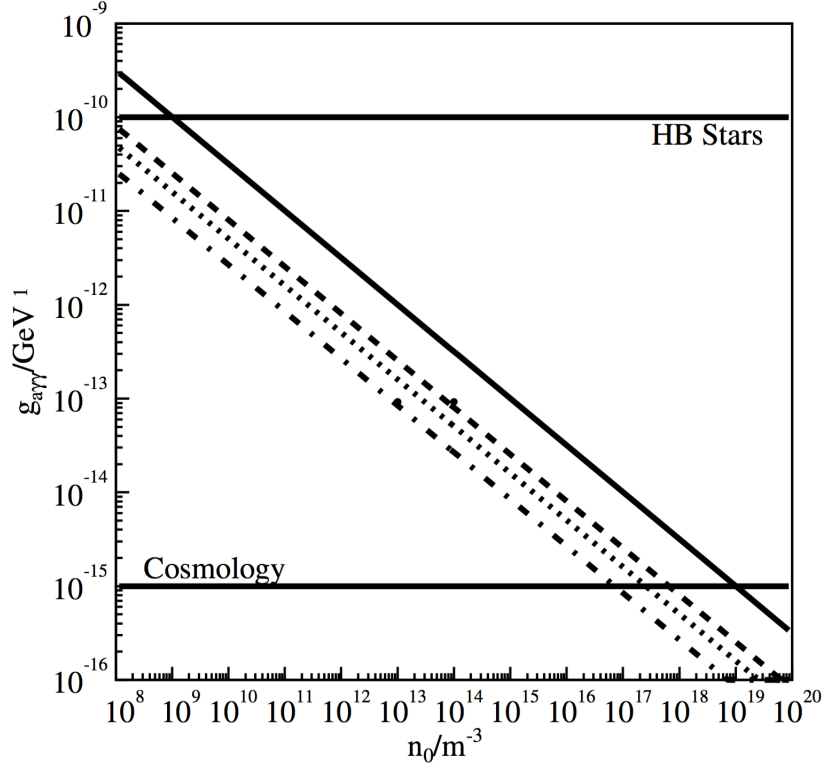
Figure 4.10: Proposed sensitivity by DRIFT experiment. Taken from [74]. Diagonal lines shows the proposed sensitivities by DRIFT. Solid one shows without-shield case, and others are with-shield cases. Horizontal line indicated as "HB Stars" shows the upper limit from the horizontal branch stars. Another line indicated as "Cosmology" shows the lower limit for axion as the dark matter. If $g_{a\gamma\gamma}$ is smaller than this line, axion would overclose the Universe.

MicroMEGAS [75], DRIFT experiment [74], and NEWS-SNO experiment [76]. Also, there are interpreted limit using the results of solar axion search experiments such as CAST [77, 78]. However, no experimental search has been carried out yet. Figure 4.10 shows the estimated sensitivity by the DRIFT experiment. For the constraints from HB stars and Cosmology in the figure, see Section 2.4.

4.2.3   Annual modulation of solar KK axion signal

Figure 4.6 shows the expected number density of the solar KK axions against the distance from the Sun. The simulated distribution taken from Ref. [72] calculated up to $200R_\odot$ is fitted well by r^{-4}. Since the Earth's obit around the Sun is elliptical, the distance between the Earth and the Sun varies in a year. From

that, we can expect an annual modulation of solar KK axion signal. The expected annual modulation is calculated as following.

First, the distance between the Earth and the Sun $r(t)$ is denoted as

$$r(t) = a \left(1 - e \cos \frac{2\pi(t - t_0)}{T} \right), \tag{4.3}$$

where $a = 1.496 \times 10^8 \, \text{km} = 215.0 R_\odot$ and $e = 0.0167$ are the semi-major axis and the eccentricity of the Earth's obit, respectively. t and T are the date and the year in days. t_0 represents the date when the Earth is at the perihelion.

Then, since it can be fitted with r^{-4} curve, the number density of trapped KK axion $n_a(t)$ becomes

$$\begin{aligned} n_a(t) &= \bar{n}_a \left(1 - e \cos \frac{2\pi(t - t_0)}{T} \right)^{-4} \\ &\approx \bar{n}_a \left[1 + 4e \left(\cos \frac{2\pi(t - t_0)}{T} + \frac{5}{2} e^2 \cos^2 \frac{2\pi(t - t_0)}{T} \right) \right]. \end{aligned} \tag{4.4}$$

Here, $\bar{n}_a$ is the KK axion number density when $r(t) = a$. From Equation (4.4) and Figure 4.6, the number density of trapped KK axion on the Earth is calculated as $4.36 \times 10^{13} \, \text{m}^{-3}$ at the perihelion and $3.81 \times 10^{13} \, \text{m}^{-3}$ at the aphelion. From Equation (4.2), the expected event rate is proportional to the square of the KK axion-photon coupling $g'_{a\gamma\gamma}$ and the number density n_a. From Equations (4.4) and (4.2), Figure 4.9 can be scaled corresponding to the event rate at the perihelion and the aphelion, respectively. The upper graph of Figure 4.11 shows the expected energy spectra by the trapped solar KK axion at the perihelion and the aphelion. Here, the KK axion-photon coupling $g'_{a\gamma\gamma} = 9.2 \times 10^{-14} \, \text{GeV}^{-1}$ and $n_a = 4.36 \times 10^{13} \, \text{m}^{-3}$ are assumed for the perihelion, while $n_a = 3.81 \times 10^{13} \, \text{m}^{-3}$ is assumed for the aphelion. The difference of the two spectra shown in the upper panel of Figure 4.11 is shown in the lower panel of Figure 4.11. The shape of the spectrum is assumed to be same throughout the year.
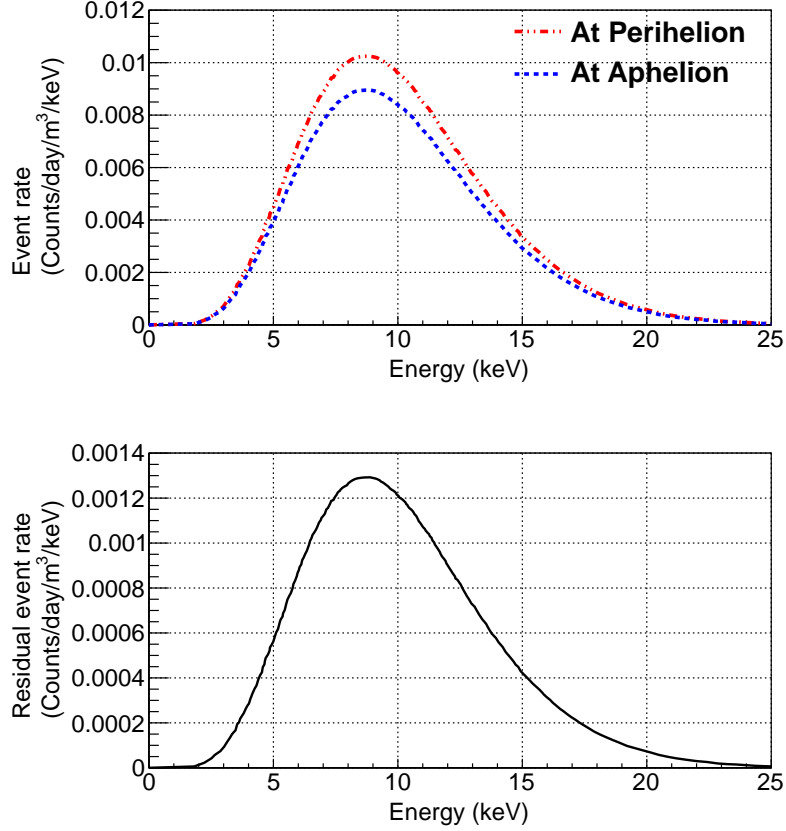
Figure 4.11: Expected energy spectra of the sum of the two photons by the decay of the trapped KK axions. Red dash-dotted curve and blue dotted curve in the upper panel show expected event rate at the perihelion and the aphelion, respectively. The black curve in the lower panel shows the expected residual event rate (difference between the perihelion and the aphelion). Here, the energy spectrum curve taken from Ref. [74] is scaled according to the density at the Earth's position. KK axion-photon coupling $g'_{a\gamma\gamma} = 9.2 \times 10^{-14}$ GeV^{-1} is assumed for both the perihelion and the aphelion. KK axion number density $n_a = 4.36 \times 10^{13}$ m^{-3} and $n_a = 3.81 \times 10^{13}$ m^{-3} are assumed for the perihelion and the aphelion, respectively.

5

The XMASS-I Detector

5.1 The XMASS experiment

The XMASS experiment is a multipurpose experiment using liquid xenon (LXe), which is sensitive to keV - MeV physics such as dark matter, neutrinoless double beta decay, and solar neutrino. Thus the name "XMASS" has following meaning:

- Xenon Detector for Weakly Interacting Massive Particles

- Xenon Neutrino Mass Detector

- Xenon Massive Detector for Solar Neutrino.

Not only these physics targets, but even more topics such as solar axions, double electron capture, super WIMPs, hidden photons and so forth are being studied by XMASS.

XMASS project has three phase called "XMASS-I", "XMASS-1.5", and "XMASS-II". Now the XMASS-I is running [79] and we use data taken by XMASS-I in this study. The detector is located 2700 m water equivalent underground in Laboratory C at Kamioka Observatory in Japan.

Detector refurbishment

The XMASS-I detector was refurbished from May 2012 to November 2013 to reduce backgrounds found in the commissioning run. In this study we use the data after the refurbishment (RFB). The geometry of the detector described here is also that of after the refurbishment.
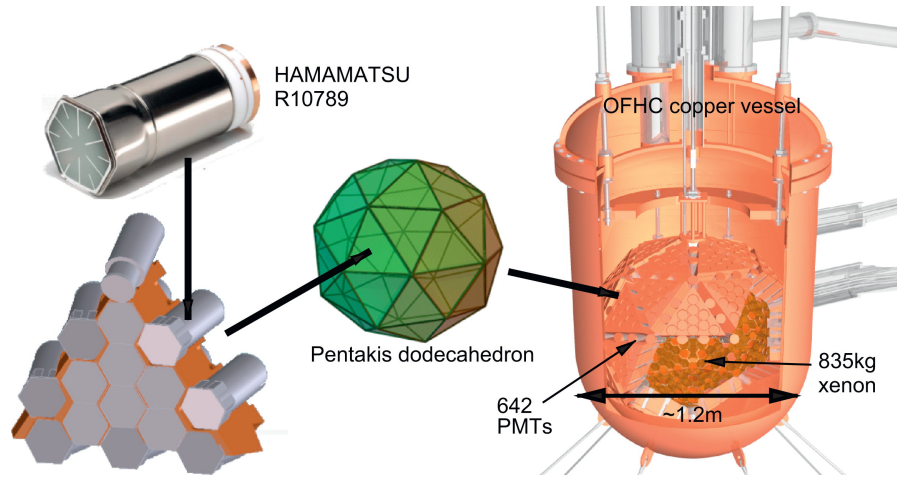
Figure 5.1: Schematic view of XMASS detector.

Figure 5.2: XMASS detector in the water tank

5.2 The inner detector

The inner detector (ID) consists of a pentalkis-dodecahedron-shaped OFHC copper holder, 642 inward-looking photomultiplier tubes (PMTs), and liquid xenon (Figure 5.1). They are insulated from the outside by a OFHC copper vessel which consists of an inner vacuum chamber (IVC) and an outer vacuum chamber (OVC). 642 Hamamatsu R10789-11 PMTs are used for the inner detector of XMASS. They detect the scintillation lights from liquid xenon. Sensitive mass of liquid xenon is 832 kg, and its volume is 0.288 m^3.

Liquid xenon

XMASS-I is a single phase liquid xenon detector. Liquid xenon has following good features.

- It has high scintillation yield.

- Scintillation light has a wavelength of $\sim$ 175 nm which is observable by PMTs without wavelength shifters.

- There is no long-lived isotopes (except nuclei which undergo double-beta decay or double electron capture with very long half-lives).

- Purification by distillation is easy.

- Large atomic number Z is good for Spin-Independent WIMP search.

- High density and high Z realize effective self-shielding against gamma rays.

- Operating temperature (~ -100 C°) is not too low and relatively easy to handle.

By these reasons, liquid xenon is an ideal material for low background experiments such as dark matter, double beta decay and solar neutrino physics [80].

5.3 The outer detector

The ID is placed in an outer detector (OD) which is a water tank 10.5 m in height and 10 m in diameter (Figure 5.2). The OD has 72 20-inch PMTs (Hamamatsu R3600) and it works as a Cherenkov veto counter. In addition, it works as a passive shield against neutrons and gamma rays from the rock in the mine.
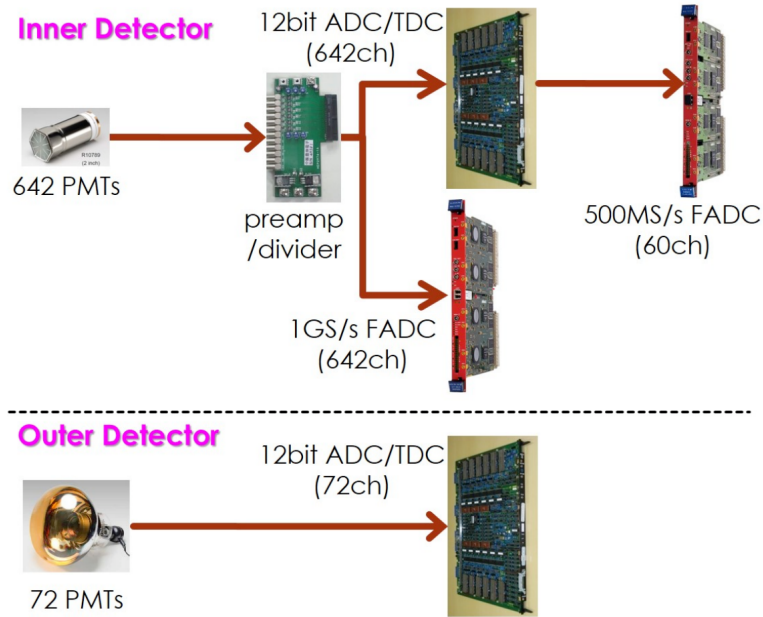
Figure 5.3: Schematic diagram of the readout electronics of XMASS. Taken from [81].

5.4   Data acquisition system

Data from PMTs are collected by ATM (analogue timing module) and FADC (flash analogue to digital converter, CAEN V1751) [81]. The threshold for an ID PMT is set at 0.2 photoelectron (PE). A trigger is issued when four or more PMT detect signals exceeding the threshold within 200 ns. The schematic diagram of electronics is shown in Figure 5.3.

5.5   Calibrations

5.5.1   LED calibration

The gain of a PMT is monitored by LEDs installed in the inner detector. Those LEDs are flashed at 1 Hz by a LED tigger. The LED calibration is automatically performed during the physics runs and the LED events are easily distinguished by their trigger types.

Table 5.1: Radioacitive sources used for the inner calibration and their photon energy.

^{55}Fe	5.9 keV
^{57}Co	122 keV
^{241}Am	17.8 keV, 59.5 keV

5.5.2 Inner calibration

The detector is calibrated by inserting radioactive sources into the liquid xenon. This calibration method is called inner calibration [79]. The radioactive sources used for the inner calibration are listed in Table 5.1 together with their photon energies [82]. The inner calibration provides us with detailed information about the detector such as the energy scale, the position dependence of photoelectron yields, and so on. The inner calibration with a ^{57}Co source is conducted weekly. In this study, the energy scale measured by a ^{57}Co source in each calibration run is used.

5.5.3 Outer calibration

The detector can also be calibrated by the irradiation with gamma rays from the source placed outside of the copper vessel. This calibration method is called the outer calibration and it is used for monitoring the change of photon yield and studying the detector response to the external radiation. Radioactive sources such as ^{60}Co, ^{137}Cs and ^{232}Th are used. We introduce the source from the inlet on the top of the water tank and transport in the guide tubes placed in the water. There are two kinds of guide tubes for the outer calibration (Figure 5.4). We can place the source anywhere in the thicker tube ($\varnothing$48 mm). Thinner one ($\varnothing$12 mm) is newly designed and installed by the author during the refurbishment of the detector with a simple structure so that the calibration can be conducted easily. Outer calibration with a ^{60}Co source using the thin tube is usually conducted weekly, and occasionally it can be conducted even more frequently in case of rapid change of photon yield. Outer calibration does not provide detailed information like inner calibration, but it can be performed much easier and has less effect on the detector. Because of these features, outer calibration is convenient to know the stability of the detector, which is described in Section 6.1.

5.5.4 Energy scale

In this paper, an energy scale keV$_{ee}$ represents the electron equivalent energy. The photoelectron yield is measured by 122 keV of ^{57}Co inner calibrations. From
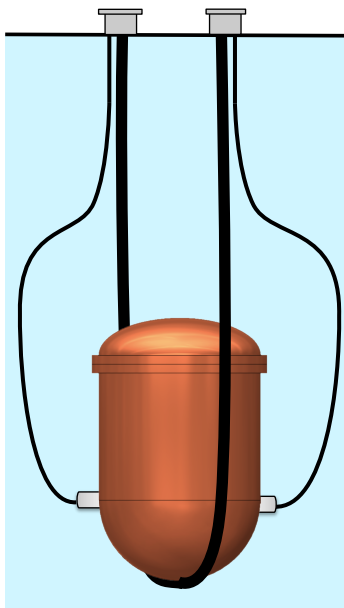
Figure 5.4: Outer calibration system

the number of photoelectrons corresponding to 122 keV, we obtain photoelectron yield per keV (PE/keV_{57Co}). Since keV_{57Co} is an XMASS-specific unit, we convert it to keV_{ee} by using the XMASS detector simulation described in the next section. We generate photon events with certain energy such as 1 keV, 10 keV, ... These energies are written as keV_{ee}. From the number of photoelectrons we observed in the simulation, we calculate the energy in keV_{57Co} corresponding to the initial energy in keV_{ee}. Thus we obtain a conversion function from keV_{57Co} to keV_{ee} shown in Figure 5.5.

There is a non-linearity in the scintillation yield of LXe. This effect on the energy scale was taken into account in the Monte Carlo simulation using the calibration results and the non-linearity model from Doke et al. [83]. The photoelectron yield below $5.9\,keV_{ee}$ was estimated by an extrapolation based on the same model.

5.6   Detector simulation

Detailed detector Monte Carlo (MC) simulation based on Geant4 [84] has been developed by the XMASS collaboration. This MC plays many important roles in XMASS, such as

- To evaluate BG components and their event rate.

- To evaluate cut efficiencies.
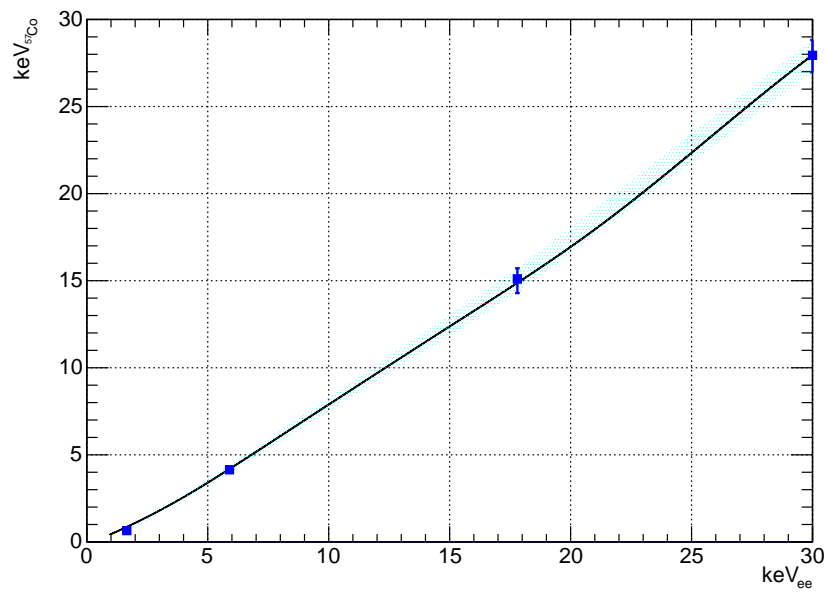
Figure 5.5: The conversion function from $keV_{^{57}Co}$ to keV_{ee}. The black solid line is the conversion function obtained from the simulation. The blue data points at 1.65 keV_{ee}, 5.9 keV_{ee}, 17.8 keV_{ee} show the calibration points. From the errors of those calibrations, we set the error band shown in the cyan band.
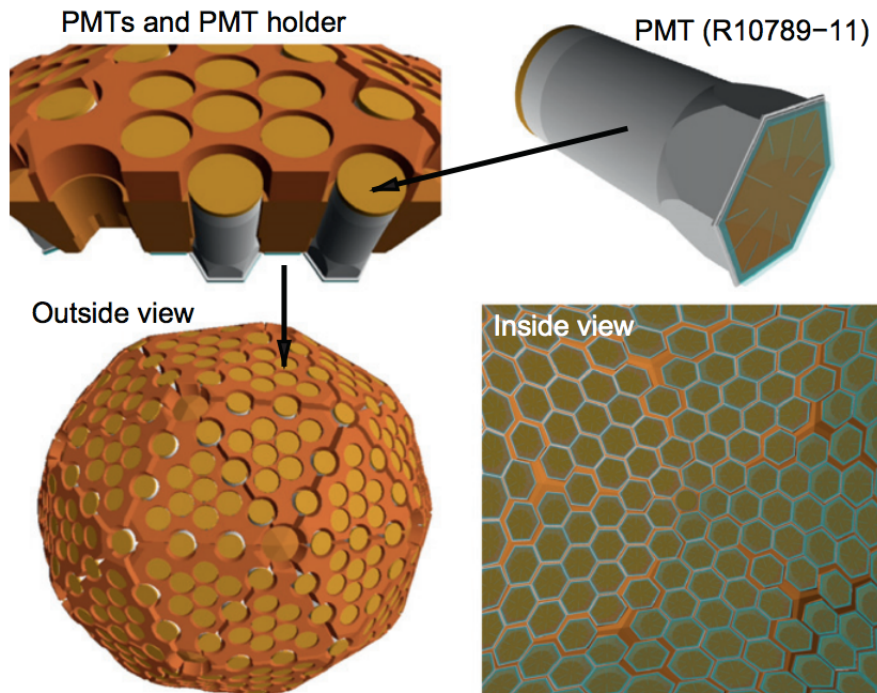
Figure 5.6: Schematic drawing of the XMASS detector MC simulation.

- To obtain optical parameters of liquid xenon and other detector materials.

There are two main optical parameters for liquid xenon, the absorption length and the scattering length. They are affected by the change of the purity of liquid xenon. Regular calibration provides us with the time variation of those values. The schematic drawing of the MC simulation geometry is shown in Figure 5.6. The MC includes detailed structures of the detector and every photon generated in the MC event is traced.

6

KK axion search with XMASS-I

6.1 Measurement and data quality

The data for this study were taken between November 2013 and March 2015. The exposure is 832 kg $\times$ 359 live days. The live time of the data after the quality check together with real elapsed time is shown in Figure 6.1.

By the weekly ^{57}Co calibration, about 10% variation of photoelectron yield was observed during the measurement period. By using Monte Carlo simulation of the XMASS detector, this change was found to be due to the change of the liquid xenon absorption length. While the absorption length varied from about 4 m to 11 m, the intrinsic light yield of the liquid xenon stayed in $\pm \sim 1\%$ (Figure 6.2).

6.2 Analysis

6.2.1 Event selection

Event selection applied in this study is summarized in this section.

Preselection

We select events triggered only by the ID. The analysis threshold for the number of PMT hits is four. Also, we eliminate electronic noise events before applying following cuts. This cut step is indicated as Cut (1) in this thesis. The distribution of the number of PMT hits for observed data is shown in Figure 6.3.

Time difference cut

We require the time difference from the previous event is more than 10 ms. The distribution of the time difference of events for observed data is shown in Figure 6.4.
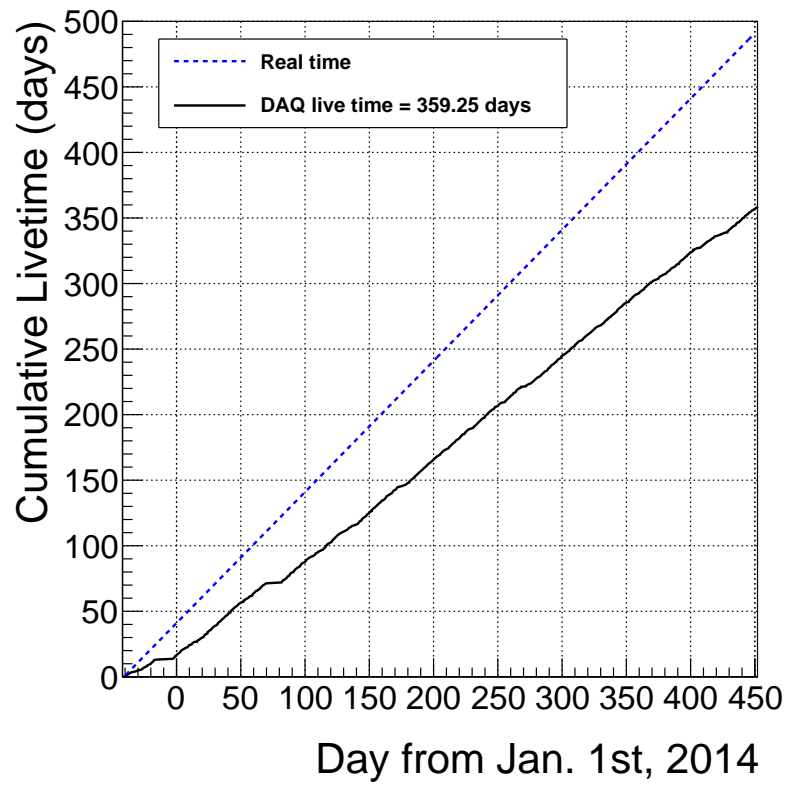
Figure 6.1: Accumulation of data from Jan. 1st, 2014. Live time of data is shown in black solid line. Blue dotted line shows the elapsed time.
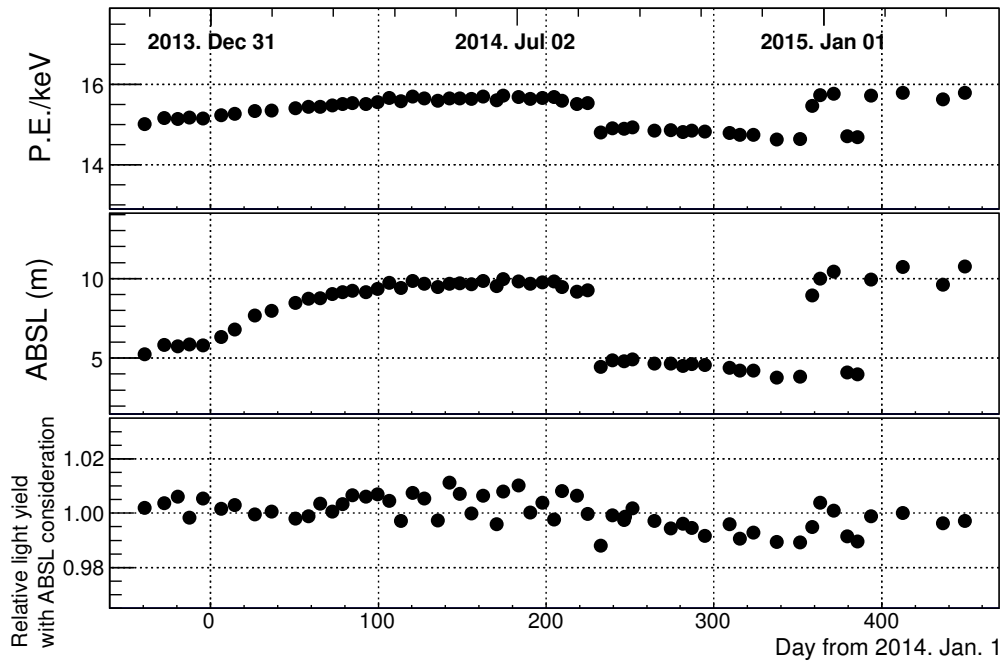
Figure 6.2: The time variation of the photoelectron yield (top), the absorption length (middle), and the relative intrinsic light yield (bottom). While the absorption length varied from about 4 m to 11 m, the intrinsic light yield of the liquid xenon stayed in $\pm \sim 1\%$
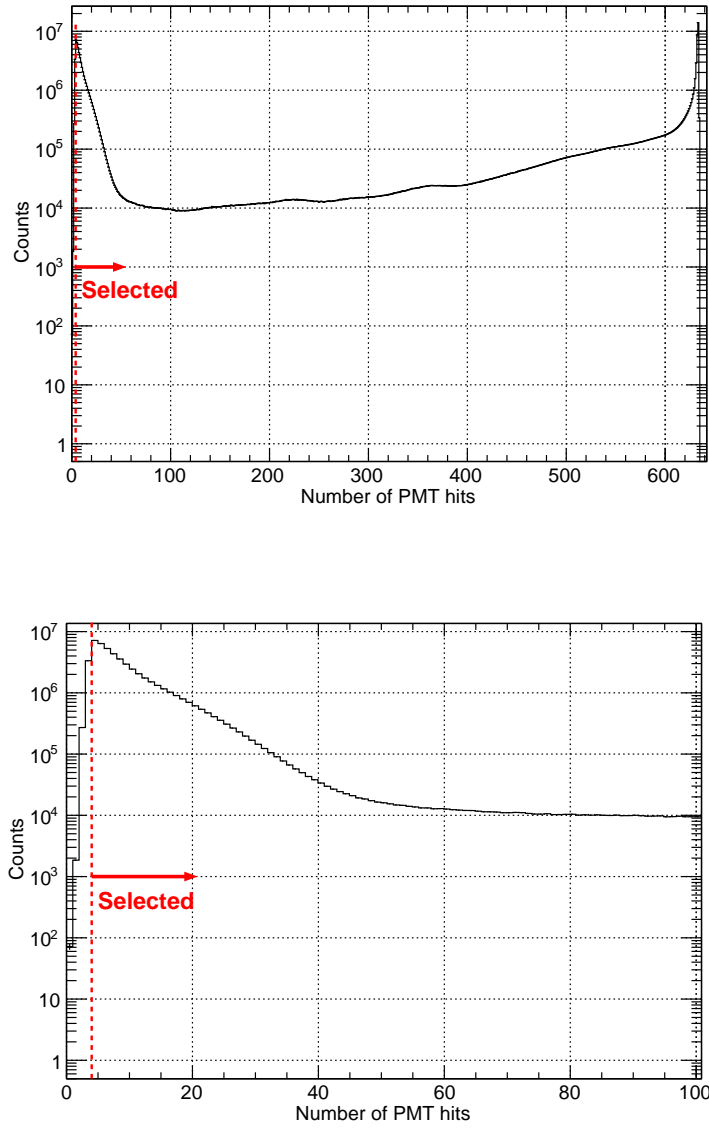
Figure 6.3: The distribution of the number of PMT hits for observed data. The lower figure is zoomed one of upper one. The red dotted line shows the threshold.

Time RMS cut

We select events whose root mean square (RMS) of hit timings is less than 100 ns. The time difference cut and the time RMS cut are both for cutting out afterpulse events and are indicated as Cut (2) in this thesis. The distribution of the time RMS for observed data are shown in Figure 6.5.

Cherenkov cut

We select events whose ratio of the number of hits in the first 20 ns to the total number of hits is less than 0.6 in order to remove Cherenkov events originated from ^{40}K in the photocathodes of PMTs. This cut is applied only to the events with the total number of PE less than 200. The cut is named Cherenkov cut and it is indicated as Cut (3) in this thesis. The distribution of the ratio is shown in Figure 6.6.

Max PE cut

Max PE cut is used to cut off the events which occurred in front of the PMTs , or "the surface of the detector". Max PE ratio r_{max} is defined as follows.

$$r_{\mathrm{max}} = \frac{\text{Number of PEs from the PMT which has the largest value in PE}}{\text{Total number of PEs from the all PMTs which have hit}} \quad (6.1)$$

If r_{max} is large, the possibility that the event occurred in the surface is large. We cut off the events whose r_{max} is larger than certain PE-dependent cut value shown in Fig 6.7. The Max PE cut is indicated as Cut (4) in this thesis. The distribution of the ratio is shown in Figure 6.8.

The observed energy spectrum used for this study after each cut step described above is shown in Figure 6.9. Here, the number of events is normalized using the unit Counts/day/kg/keV$_{\mathrm{ee}}$.

6.2.2 KK axion signal simulation

By inputting the decay spectra of the KK axion in Figure 4.9 to the MC of our detector, we made the energy spectra of the expected signal for a given time of the day. Figure 6.10 shows the energy spectrum and efficiencies after each cut of KK axion signal MC.

6.2.3 Systematic uncertainties

We have three main components of the systematic uncertainties on this study.
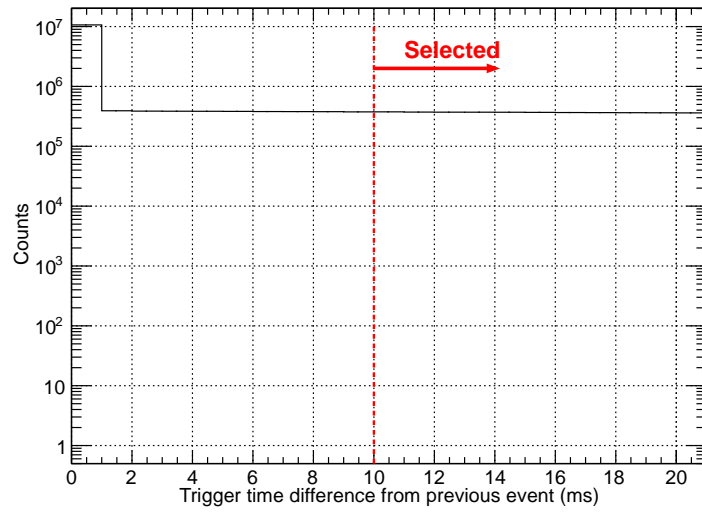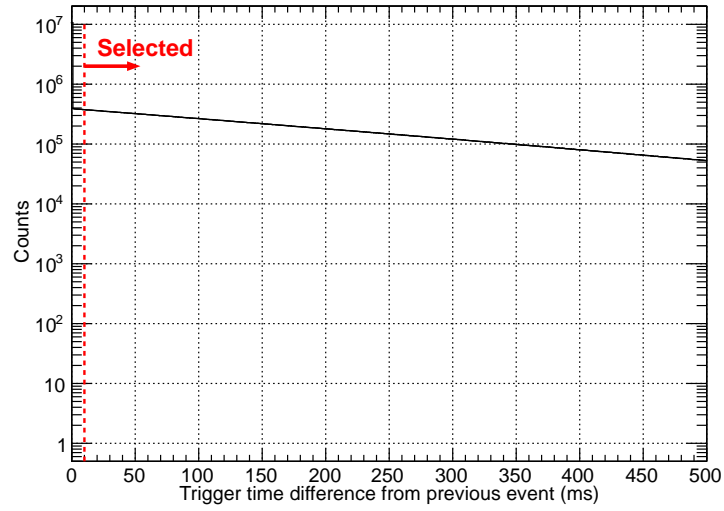
Figure 6.4: The distribution of the time difference from the previous events for observed data. The lower figure is zoomed one of upper one. The red dotted line shows the cut value.
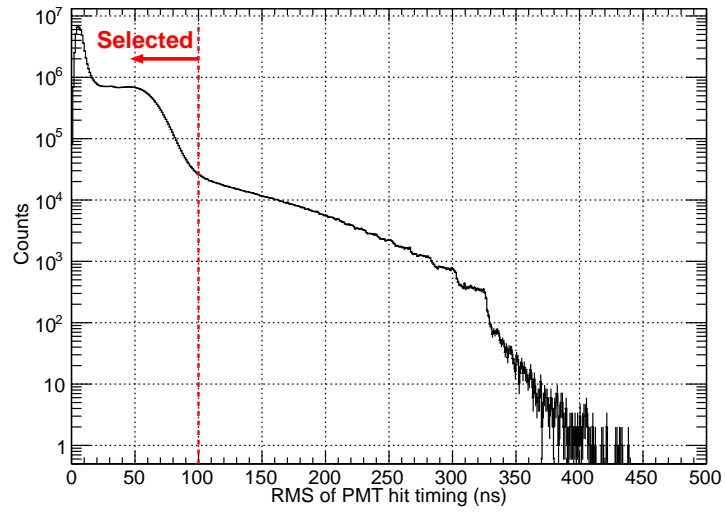
Figure 6.5: The distribution of RMS of the hit timing for observed data. The red dotted line shows the cut value.
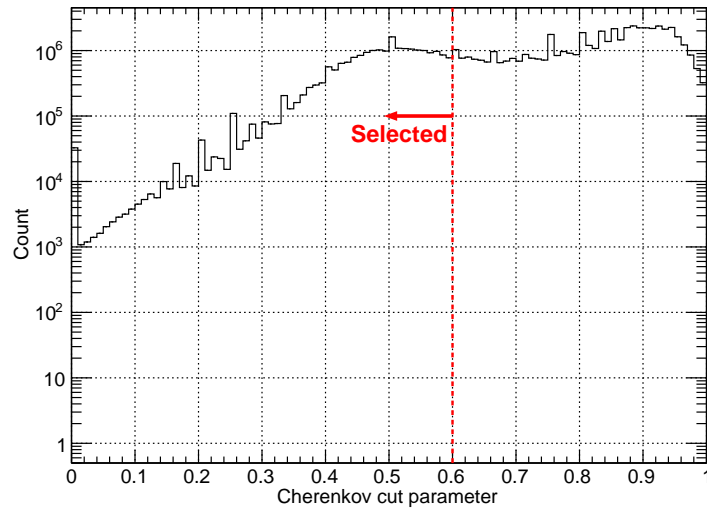
Figure 6.6: The distribution of the ratio of the number of hits in the first 20 ns to the total number of hits for observed data. The red dotted line shows the cut value.
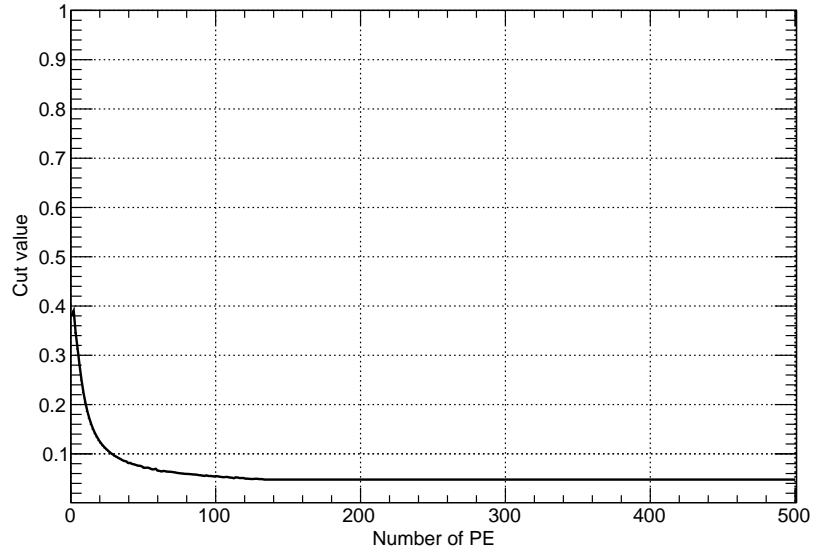
Figure 6.7: The cut value for Max PE ratio.
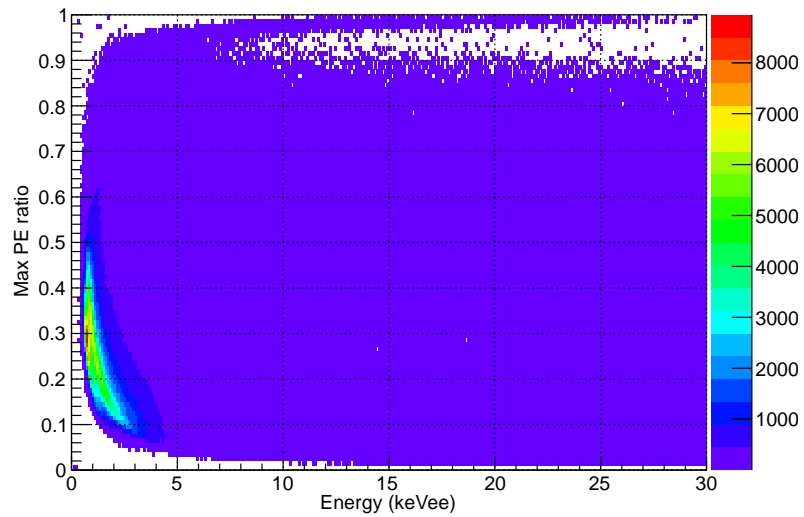
Figure 6.8: The distribution of the Max PE ratio VS energy for observed data.
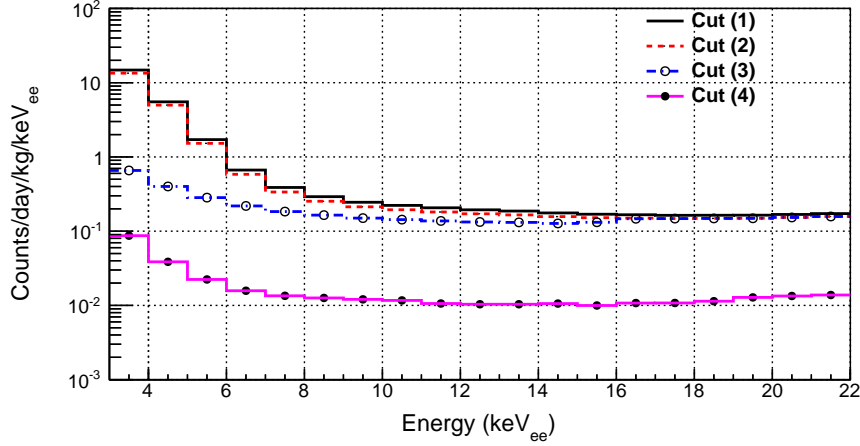
Figure 6.9: The observed energy spectrum used for this study. Each line corresponds to the event rate after each cut step described in the text. The live time of this data is 359 days.

Cut efficiency

The largest systematic error comes from the variations of the cut efficiency. The cut efficiency is affected by the variation of the photoelectron yield. We corrected this effect with the relative cut efficiency evaluated by MC simulation. Using our detector MC, we simulate the change of cut efficiency against background events. By the study based on measurements with germanium detectors and the detector MC, dominant background events are found to come from following three components.

- ^{238}U $-^{230}$Th in the aluminum sealing parts of the inner detector PMTs.

- ^{210}Pb in the aluminum sealing parts of the inner detector PMTs.

- ^{210}Pb in the copper plates on the surface of the inner detector.

The aluminum sealing parts are used between the quartz window and the body part of an inner detector PMTs. After we found their contamination in the commissioning run, we deposited high-purity aluminum vapor over the sealing and covered them by copper rings (Figure 6.11). Despite these improvements, some part of the contribution by the aluminum remains. The copper plates were installed during the refurbishment to cover the gaps between inner detector PMTs, so that scintillation lights from the gap do not leak into the inner side of the detector (Figure 6.12). The energy spectra after cuts described in Section 6.2.1 from
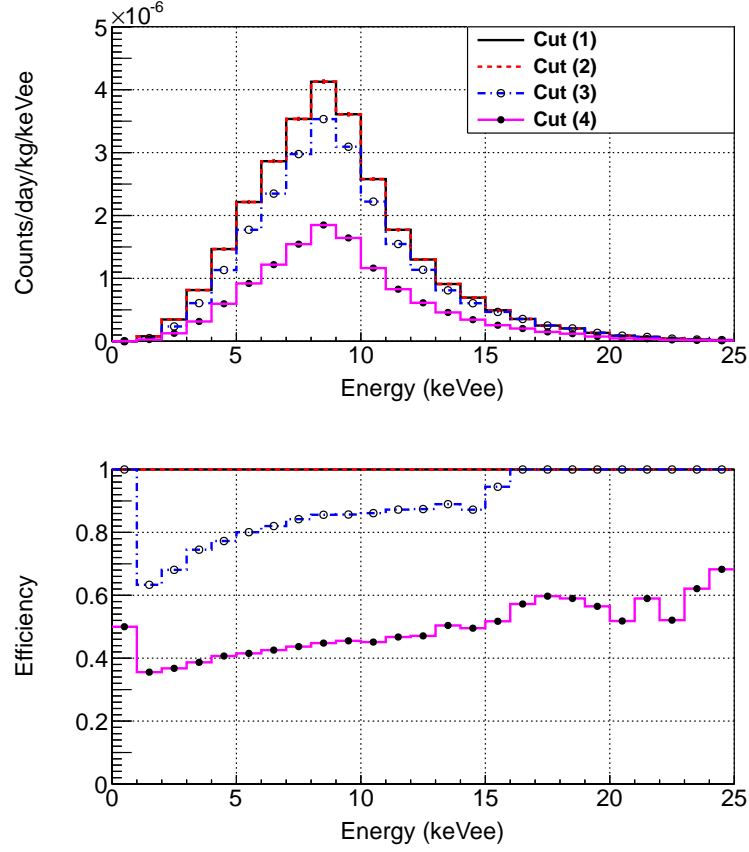
Figure 6.10: The expected energy spectrum and the selection efficiency of the KK axions signal evaluated by MC. The histogram with black solid line shows the events after cut (1). Red dotted line shows the events after cut (2). Blue dash-dotted line represents the events after cut (3). Magenta solid line with filled circle shows the events after cut (4), which are the final samples. Here, $g'_{a\gamma\gamma} = 9.2 \times 10^{-14}\,\mathrm{GeV}^{-1}$ and $n_{\mathrm{a}} = 4.07 \times 10^{13}\,\mathrm{m}^{-3}$ are assumed.
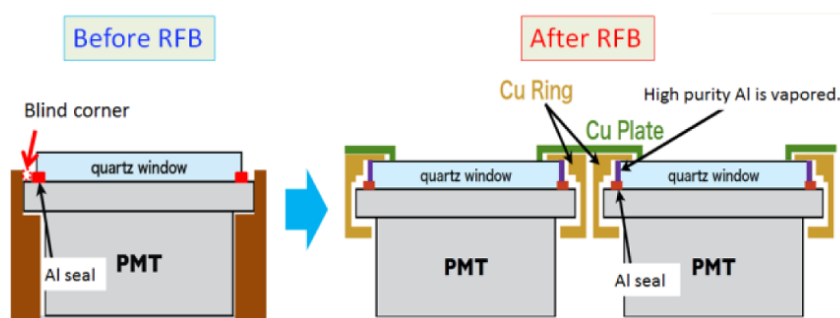
Figure 6.11: Schematic view of the aluminum sealing part of a PMT before and after the detector refurbishment. Taken from [85].
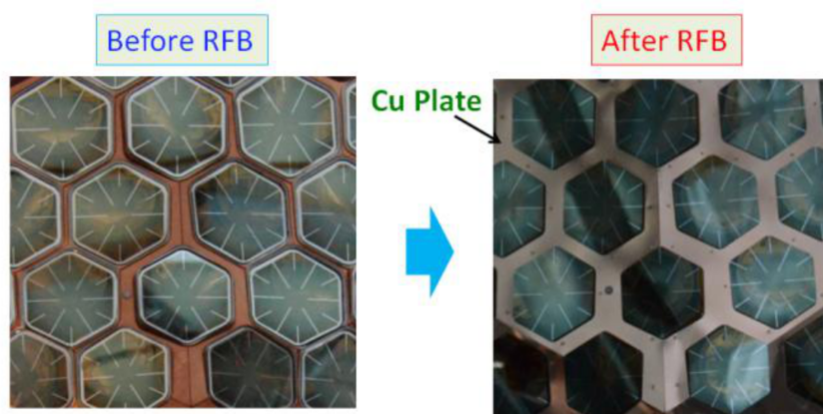
Figure 6.12: The copper plates installed on the inner surface of the detector. Taken from [85].

these three components are shown in Figure 6.13. This summed spectrum explains the shape of the spectrum observed by XMASS (Figure 6.9).

To evaluate cut efficiencies, MC events are created with different absorption length from 400 cm to 2000 cm for each BG component. Each BG component is summed up corresponds to its amount like Figure 6.13. Then, the cut efficiencies relative to the MC with absorption length of 800 cm were evaluated in three energy regions, $3 - 7$, $7 - 14$, $17 - 22$ keV$_{ee}$ (Figure. 6.14). There is an uncertainty in the shape of the aluminum sealing part of the PMTs. Since we cannot measure the shapes of 642 PMTs, we assumed two models of the aluminum sealing. We treat the difference of cut efficiency caused by the difference between these models as a systematic uncertainty. The difference of maximum and minimum was set to the systematic error band as shown in Figure 6.14, and it is taken into account in
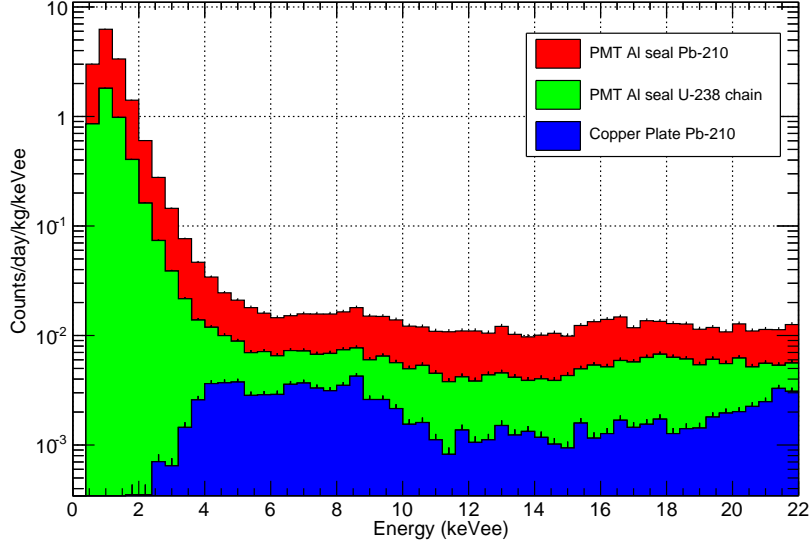
Figure 6.13: Energy spectrum from main BG components obtained from XMASS BG MC. The cuts described in Section 6.2.1 are applied.

the fitting as K_{ij} term in Equation (6.2). The uncertainty of the cut efficiency is evaluated and found to be the largest systematic error ($\pm 5\%$).

Non-linearity of energy scale below 5.9 keV

The second largest contribution to the systematic error comes from the non-linearity of the scintillation yield described in Section 5.5.4. Below 5.9 keV, we do not have energy calibration method. We assume two models of energy scale curve which are shown in Figure 6.15. The difference of two models is set as one sigma error band. This uncertainty is taken into account in the MC of the signal expectation as L_i in Equation (6.3).

Other systematic errors

The third one is the gain instability of the waveform digitizers between April 2014 and September 2014 due to different calibration methods. This contributes uncertainty of the energy scale by 0.3%. Other uncertainties are found to be negligible.
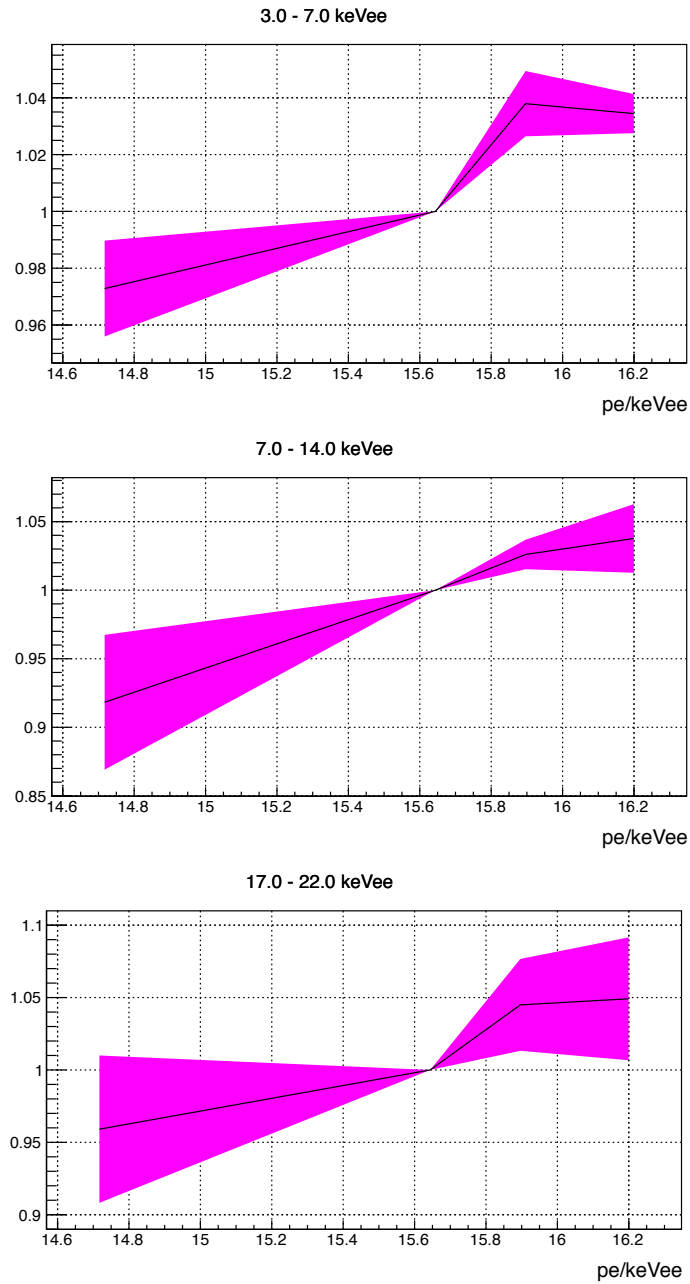
Figure 6.14: Relative cut efficiencies and their error bands in 3-7, 7-14, 17-22 keV$_{ee}$. Horizontal axis is PE yield per keV$_{ee}$ energy bins. These points are evaluated by MC with absorption length of 400, 800, 1100, and 2000 cm. Magenta error bands come from the difference between two aluminum models.
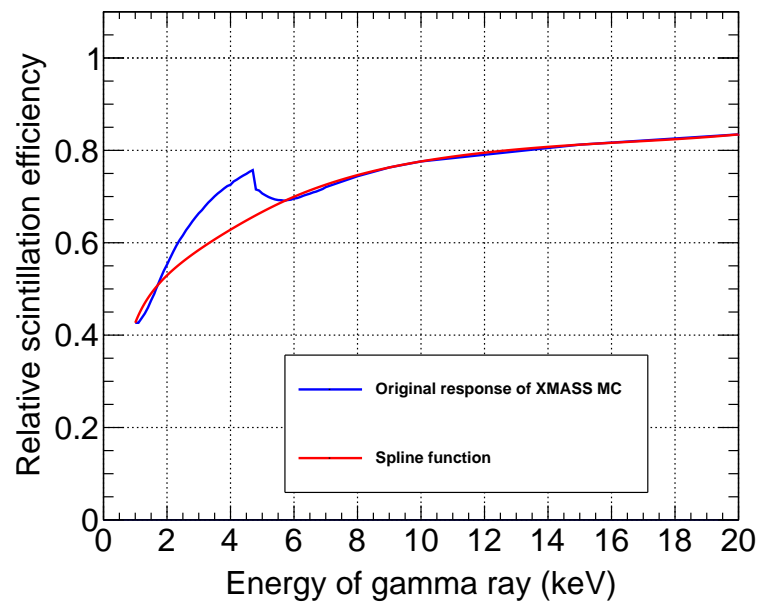
Figure 6.15: Non-linearity of the LXe scintillation efficiency. The horizontal axis is the energy of incident photon. The vertical axis is the scintillation yield of LXe relative to that of 122 keV. The blue line shows the response of XMASS MC. The red line shows the spline function extrapolated from the energy calibration results. The difference between blue and red is treated as a systematic error.

6.2.4 Annual modulation fitting

To search for the annual modulation of the KK axion signal discussed in Section 4.2.3, the following analysis is applied. The data set is divided into 33 time-bins (t_{bins}) with about 15 live-days each. Event selections summarized in Section 6.2.1 are applied, and the final data sample shown by the magenta spectrum in Figure 6.9 is used. The annual modulation amplitude is retrieved from the data with the least Chi-squares method. The data in each time-bin are divided into 16 energy-bins (E_{bins}) with a width of $1\,\text{keV}_{\text{ee}}$ each. We used two pull terms [86] of α and β in the χ^2 defined as:

$$\chi^2 = \sum_i^{E_{\text{bins}}} \sum_j^{t_{\text{bins}}} \frac{\left(R_{i,j}^{\text{data}} - R_{i,j}^{\text{ex}} - \alpha K_{i,j}\right)^2}{\sigma_{\text{stat};i,j}^2 + \sigma_{\text{sys};i,j}^2} + \alpha^2 + \beta^2, \tag{6.2}$$

where $R_{i,j}^{\text{data}}$, $R_{i,j}^{\text{ex}}$, $\sigma_{\text{stat};i,j}$, $\sigma_{\text{sys};i,j}$ are the observed event rate, the expected event rate, the statistical and the uncorrelated systematic errors, respectively. The subscripts i and j denote the energy and time bins, respectively. $K_{i,j}$ represents the 1σ correlated systematic error based on the relative cut efficiency in each period. Based on Equations (4.2) and (4.4), the expected event rate is defined as:

$$R_{i,j}^{\text{ex}} = \int_{t_j - \frac{1}{2}\Delta t_j}^{t_j + \frac{1}{2}\Delta t_j} \left[C_i + \xi \times (A_i - \beta L_i) \left(\cos\frac{2\pi(t - t_0)}{T} + \frac{5}{2}e\cos^2\frac{2\pi(t - t_0)}{T} \right) \right] dt, \tag{6.3}$$

where Δt_j is the bin width of the time bin t_j. C_i and A_i are the constant term and the expected amplitude of the event rate, respectively. A_i corresponds to the half of the residual event rate in Figure 4.11. L_i represents the uncertainty from the non-linearity of the scintillation efficiency. ξ is defined as $\xi = \frac{g_{a\gamma\gamma}'^2}{\left(9.2\times10^{-14}\,\text{GeV}^{-1}\right)^2}\frac{\bar{n}_a}{4.07\times10^{13}\,\text{m}^{-3}}$, and it represents the ratio of expected amplitudes between the data and the considering model. By treating C_i and ξ as free parameters in the fitting, the χ^2 is minimized. The data are fitted in the energy range of 3-22 keV_{ee} excluding 14-17 keV_{ee}. This exclusion is because the edge of Cherenkov cut exists in 14-17 keV_{ee} and the stability of the cut efficiency is much more largely affected by the change of the light yield than the other energy ranges.

6.3 Results

Figure 6.16-6.18 shows the event rate modulation and the best fit result of the expected event rate. As a result of the fitting, we obtain $\xi = 822$ with reduced χ^2 of 522.4/492. Using 10000 non-modulating dummy samples which have the same
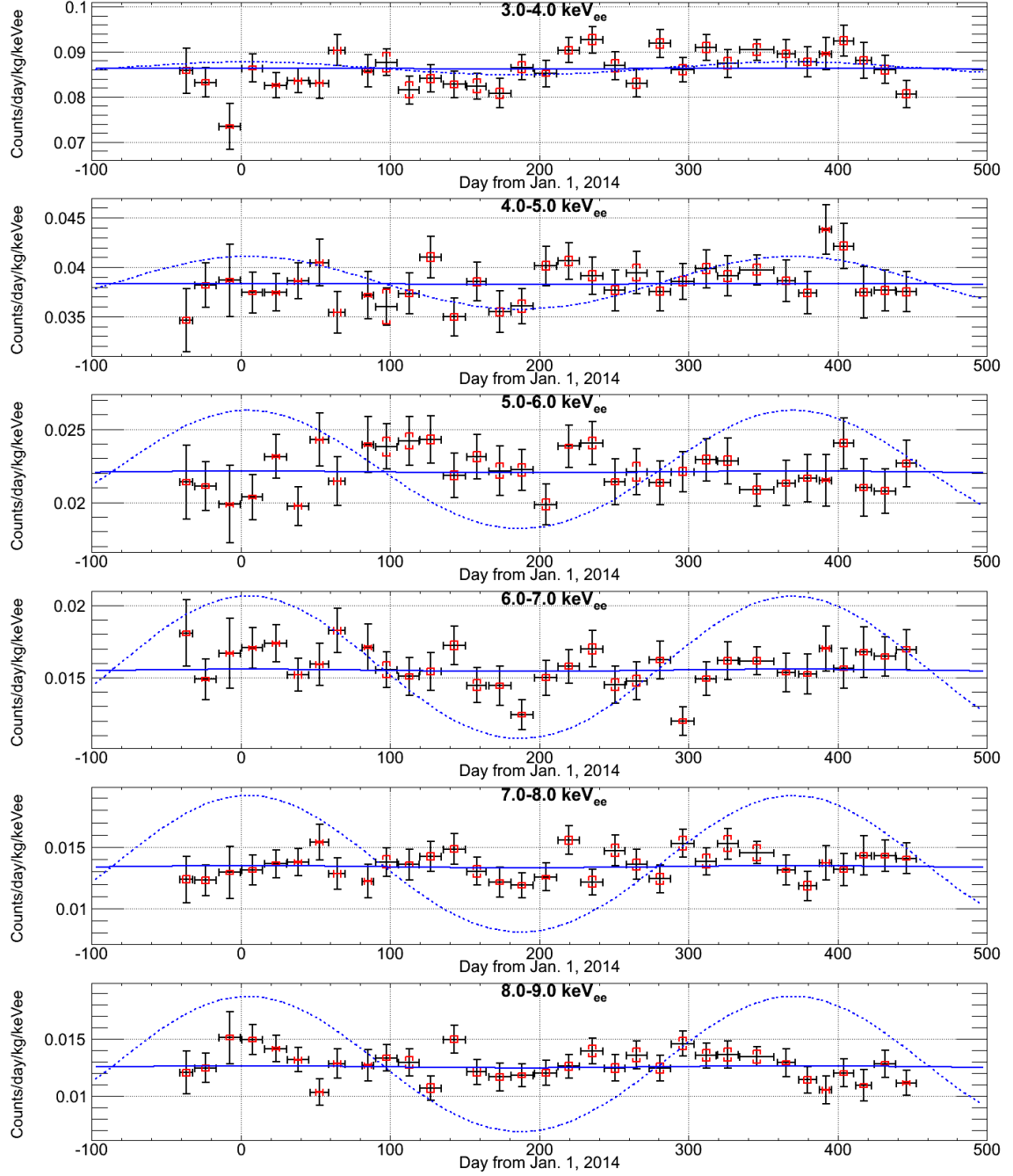
Figure 6.16: Time variation of the observed event rate in each energy bin ($3.0 -$ 9.0 keV$_{ee}$). The horizontal axis is the time defined as the number of days from January 1st, 2014. Black points with error bars show the observed event rate for each period with statistical errors $\sigma_{\mathrm{stat};i,j}$. Red error bars show the systematic errors ($\sigma_{\mathrm{sys};i,j}$ and $K_{i,j}$ are added in quadrature). Blue solid curves show the best fit result of the expected event rate variation ($\xi = 822$). Blue dotted curves show the 20 times zoomed expected amplitudes of 90% CL upper limit ($\xi = 2710$).
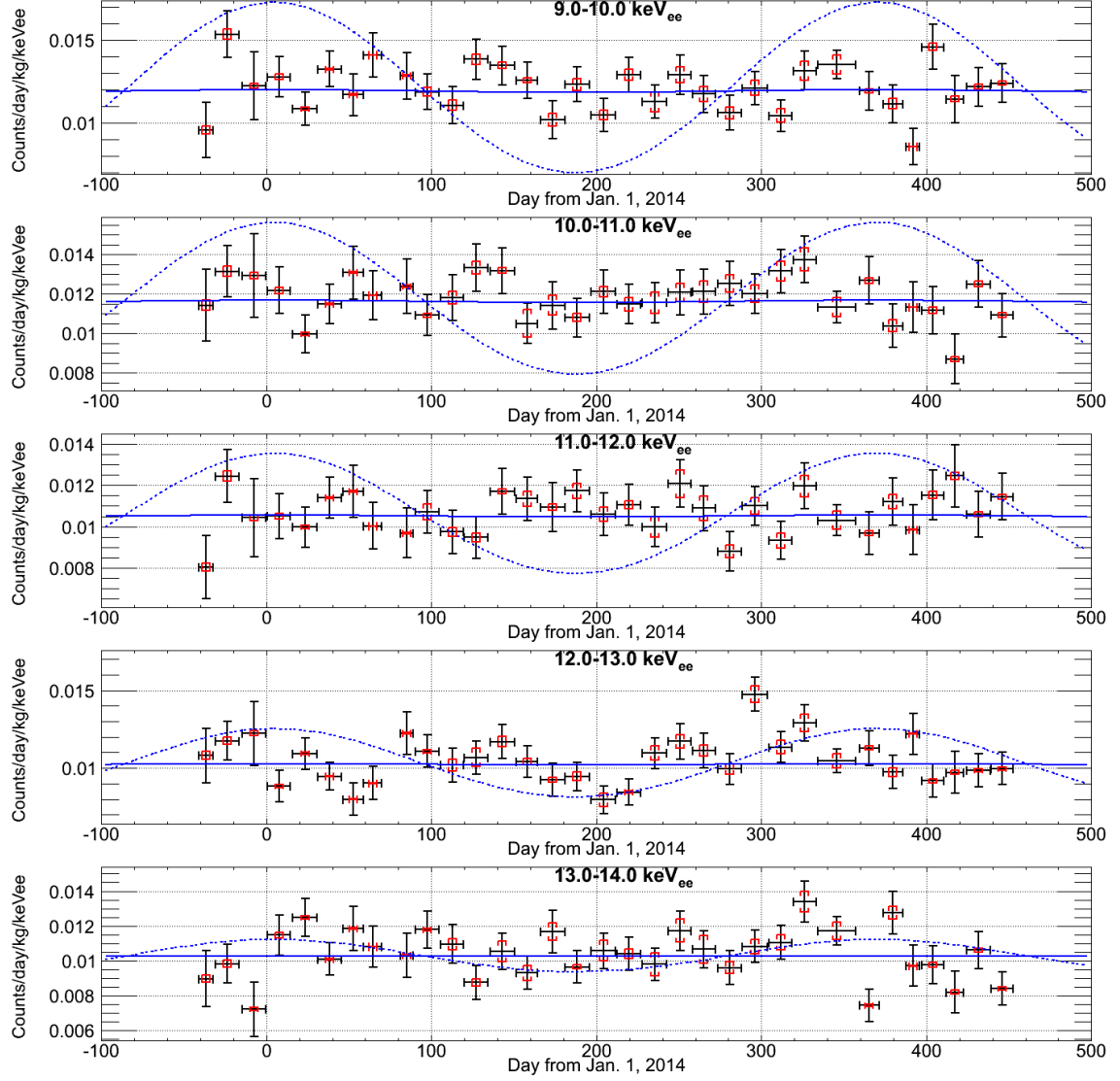
Figure 6.17: Time variation of the observed event rate in each energy bin ($9.0 - 14.0$ keV$_{ee}$). The horizontal axis is the time defined as the number of days from January 1st, 2014. Black points with error bars show the observed event rate for each period with statistical errors $\sigma_{\text{stat};i,j}$. Red error bars show the systematic errors ($\sigma_{\text{sys};i,j}$ and $K_{i,j}$ are added in quadrature). Blue solid curves show the best fit result of the expected event rate variation ($\xi = 822$). Blue dotted curves show the 20 times zoomed expected amplitudes of 90% CL upper limit ($\xi = 2710$).
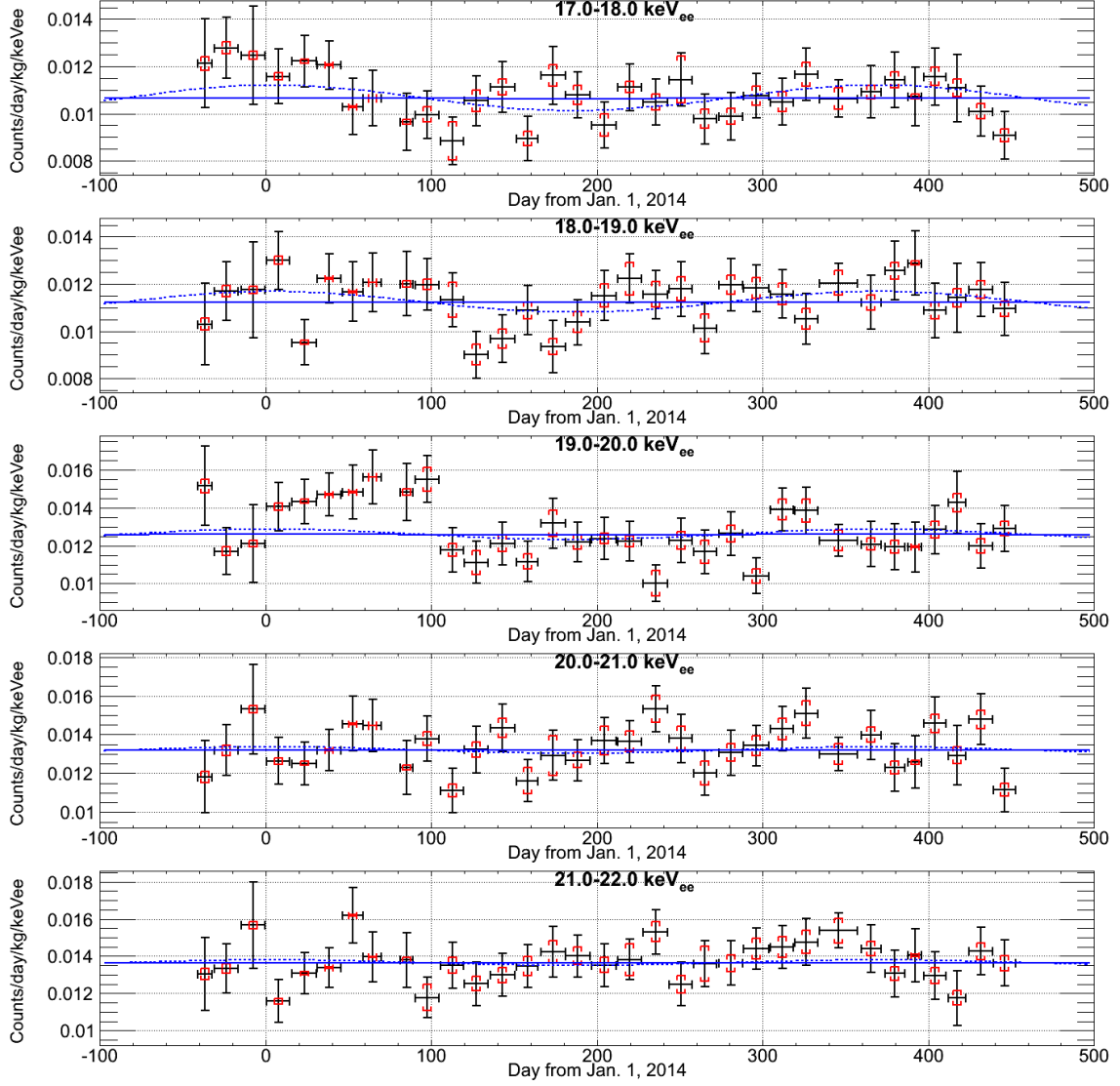
Figure 6.18: Time variation of the observed event rate in each energy bin $(17.0 - 22.0 \text{ keV}_{\text{ee}})$. The horizontal axis is the time defined as the number of days from January 1st, 2014. Black points with error bars show the observed event rate for each period with statistical errors $\sigma_{\text{stat};i,j}$. Red error bars show the systematic errors ($\sigma_{\text{sys};i,j}$ and $K_{i,j}$ are added in quadrature). Blue solid curves show the best fit result of the expected event rate variation ($\xi = 822$). Blue dotted curves show the 20 times zoomed expected amplitudes of 90% CL upper limit ($\xi = 2710$).
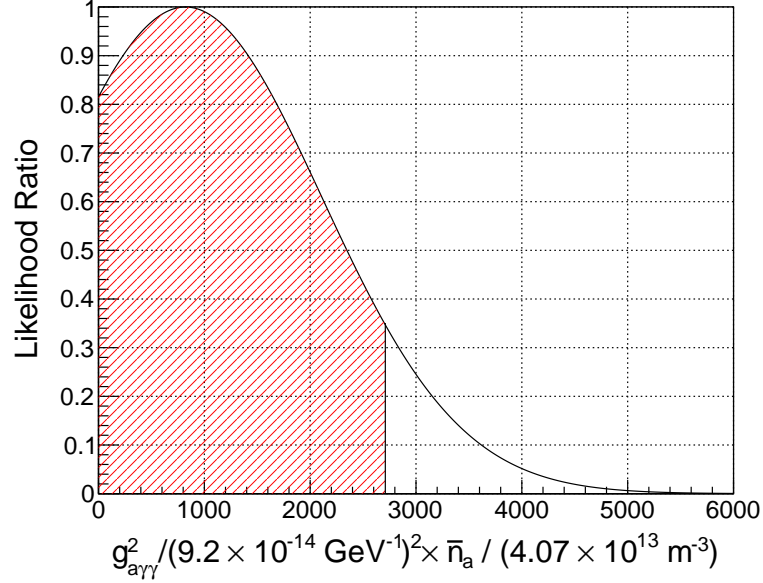
Figure 6.19: Likelihood ratio vs ξ. Best fit value of ξ is 822. The 90% C.L. upper limit of ξ is calculated as 2710.

statistical and systematic errors as data [87], we evaluated the significance of this result. By this test, p-value is evaluated as 0.62, which is not a significant value. Since no significant amplitude excess is found, a 90% confidence level (CL) upper limit is set on the KK axion-photon coupling $g'_{a\gamma\gamma}$ as a function of the KK axion number density n_a. We use the likelihood ratio $\mathcal{L}$ defined as

$$\mathcal{L} = \exp\left(-\frac{\chi^2(\xi) - \chi^2_{\min}}{2}\right),\tag{6.4}$$

where $\chi^2(\xi)$ is calculated χ^2 by varying ξ, while $\chi^2_{\min}$ is the minimum χ^2. The 90% CL upper limit is obtained by using the relation defined by Equation (6.5).

$$\frac{\int_0^{\xi_{\text{limit}}} \mathcal{L}\, d\xi}{\int_0^\infty \mathcal{L}\, d\xi} = 0.9\tag{6.5}$$

Figure 6.19 shows the distribution of likelihood ratio.

The obtained 90% CL upper limit on the coupling constant corresponding to $\xi = 2710$ is

$$g'_{a\gamma\gamma} < 4.8 \times 10^{-12} \text{ GeV}^{-1} \text{ (for } \bar{n}_a = 4.07 \times 10^{13} \text{ m}^{-3}).\tag{6.6}$$

Figure 6.20: The obtained 90% CL upper limit from this work is shown by the black solid slope and the red hatched area. The model assumed in this study based on Ref. [72] is indicated by the blue point.

This is the first experimental limit on the KK axions. This limit can be calculated for different KK axion density and the obtained limit line is shown by the black solid slope in Figure 6.20. As a bench mark, the proposed solar KK axion model ($g'_{a\gamma\gamma} = 9.2 \times 10^{-14}$ GeV^{-1}, $\bar{n}_a = 4.07 \times 10^{13}$ m^{-3}) [72] is shown in Figure 6.20.

7

Discussion

In this study, no significant excess for the annual modulation signal of solar KK axion is found and the 90% CL upper limit is set on KK axion-photon coupling $g'_{a\gamma\gamma} < 4.8 \times 10^{-12} \text{ GeV}^{-1}$ for $\bar{n}_a = 4.07 \times 10^{13} \text{ m}^{-3}$. This is the first experimental limit on the KK axions. In Figure 7.1, we compare our limit with other astrophysical and cosmological constraints. Under the assumption that the limit from HB stars is still valid despite the existence KK axions, for $n_a > 3 \times 10^{11} \text{ m}^{-3}$ we got more stringent limit than that from HB stars [88]. Note that the tension from the solar neutrino measurements as a consequence of the luminosity limit is $L_a < 0.1 L_\odot$ [89] which corresponds to $\bar{n}_a < 2 \times 10^{13} \text{ m}^{-3}$, however, there still remains allowed solar KK axion model with different values of M_F and δ as discussed in Ref. [72].

The sensitivity of this study was not enough to search the region of predicted solar KK axion model. A liquid xenon detector with a BG level less than 10^{-5} events/day/kg/keV$_{ee}$, a mass of 3 tons, and 5 years of exposure should be able to explore the predicted region. For example, a single phase liquid xenon detector with mass of 5 tons, whose fiducial volume is mass of 3 tons, will be suitable.
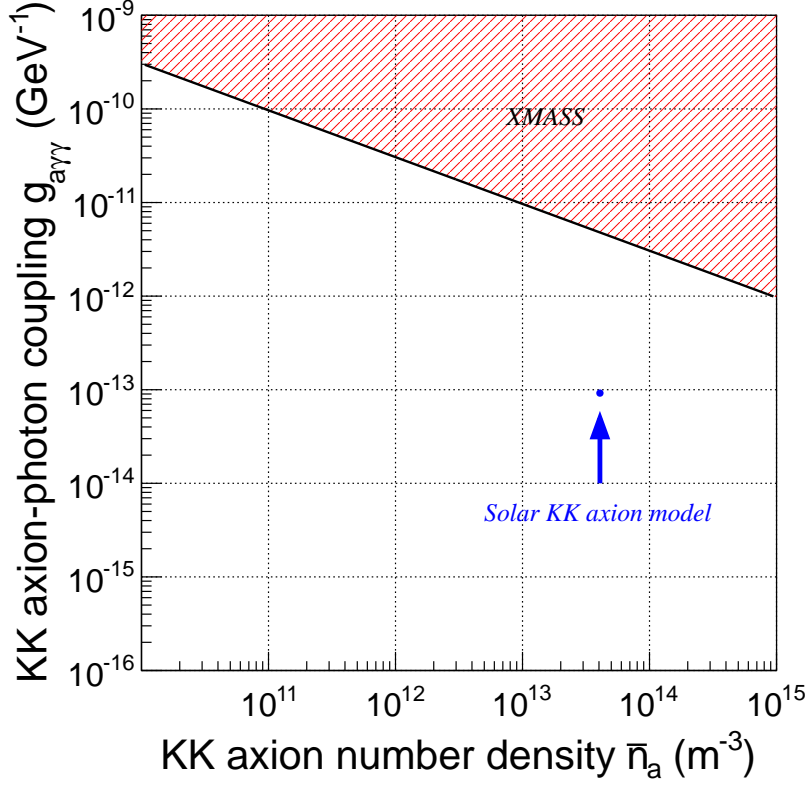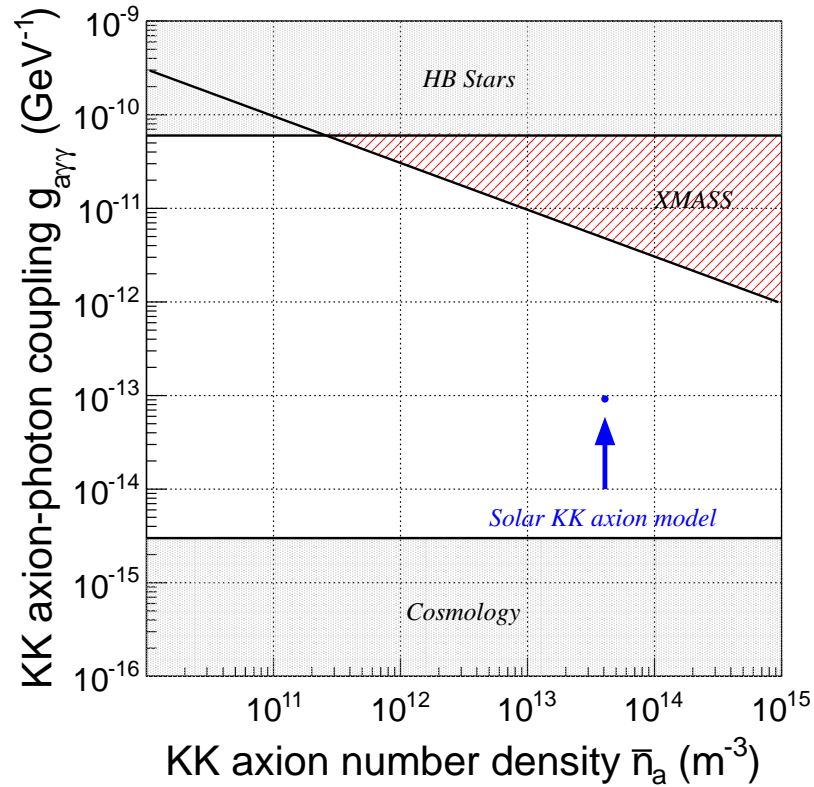
Figure 7.1: The obtained 90% CL upper limit from this work is shown by the black solid slope and the red hatched area. The model assumed in this study based on Ref. [72] is indicated by the blue point. Hatched gray areas are ruled out by HB stars [88] and Cosmology [90]. Here, we assumed that the limits from HB stars and Cosmology are still valid despite the existence KK axions.

8

Conclusion

The theories of extra dimensions are introduced to solve the gauge hierarchy problem, and axion is introduced to solve the strong CP problem. If axion propagates these extra dimensions, we would observe Kaluza-Klein modes of axion, namely KK axions. KK axions can be produced thermally in the Sun, and a small fraction of them are gravitationally trapped by the Sun. These solar KK axion would decay into two photons typically in about 10^{10} year, and the photons are in the X-ray region. These X-rays may explain the unsolved mechanism of heating of the solar corona.

In this study, the decay of the solar KK axion was searched by using 832×359 kg·days of data taken by XMASS-I, a large liquid xenon detector located at 1000 m underground in Kamioka Observatory. We performed a unique method, the annual modulation analysis. By the search, no significant excess over expected background is found, and a 90% upper limit for axion-photon coupling of $g'_{a\gamma\gamma} < 4.8 \times 10^{-12}\,\mathrm{GeV}^{-1}$ at $n_a = 4.07 \times 10^{13}\,\mathrm{m}^{-3}$ is set. This is the first experimental limit on KK axions.

Bibliography

[1] F. Halzen and Alan D. Martin. *QUARKS AND LEPTONS: AN INTRO-DUCTORY COURSE IN MODERN PARTICLE PHYSICS.* 1984.

[2] G. Aad et al. Observation of a new particle in the search for the standard model higgs boson with the atlas detector at the lhc. *Physics Letters B*, 716(1):1 – 29, 2012.

[3] S. Chatrchyan et al. Observation of a new boson at a mass of 125 gev with the cms experiment at the lhc. *Physics Letters B*, 716(1):30 – 61, 2012.

[4] Makoto Kobayashi and Toshihide Maskawa. Cp-violation in the renormalizable theory of weak interaction. *Progress of Theoretical Physics*, 49(2):652, 1973.

[5] J. M. Pendlebury, S. Afach, N. J. Ayres, C. A. Baker, G. Ban, G. Bison, K. Bodek, M. Burghoff, P. Geltenbort, K. Green, W. C. Griffith, M. van der Grinten, Z. D. Grujić, P. G. Harris, V. Hélaine, P. Iaydjiev, S. N. Ivanov, M. Kasprzak, Y. Kermaidic, K. Kirch, H.-C. Koch, S. Komposch, A. Kozela, J. Krempel, B. Lauss, T. Lefort, Y. Lemière, D. J. R. May, M. Musgrave, O. Naviliat-Cuncic, F. M. Piegsa, G. Pignol, P. N. Prashanth, G. Quéméner, M. Rawlik, D. Rebreyend, J. D. Richardson, D. Ries, S. Roccia, D. Rozpedzik, A. Schnabel, P. Schmidt-Wellenburg, N. Severijns, D. Shiers, J. A. Thorne, A. Weis, O. J. Winston, E. Wursten, J. Zejma, and G. Zsigmond. Revised experimental upper limit on the electric dipole moment of the neutron. *Phys. Rev. D*, 92:092003, Nov 2015.

[6] Maxim Pospelov and Adam Ritz. Electric dipole moments as probes of new physics. *Annals of Physics*, 318(1):119 – 169, 2005. Special Issue.

[7] R. D. Peccei and Helen R. Quinn. CP conservation in the presence of pseudoparticles. *Phys. Rev. Lett.*, 38:1440–1443, Jun 1977.

[8] Steven Weinberg. A new light boson? *Phys. Rev. Lett.*, 40:223–226, Jan 1978.

[9] F. Wilczek. Problem of strong p and t invariance in the presence of instantons. *Phys. Rev. Lett.*, 40:279–282, Jan 1978.

[10] William A. Bardeen and S.-H.H. Tye. Current algebra applied to properties of the light higgs boson. *Physics Letters B*, 74(3):229 – 232, 1978.

[11] Michael Dine, Willy Fischler, and Mark Srednicki. A simple solution to the strong cp problem with a harmless axion. *Physics Letters B*, 104(3):199 – 202, 1981.

[12] A. R. Zhitnitsky. On Possible Suppression of the Axion Hadron Interactions. (In Russian). *Sov. J. Nucl. Phys.*, 31:260, 1980. [Yad. Fiz.31,497(1980)].

[13] Jihn E. Kim. Weak-interaction singlet and strong CP invariance. *Phys. Rev. Lett.*, 43:103–107, Jul 1979.

[14] M.A. Shifman, A.I. Vainshtein, and V.I. Zakharov. Can confinement ensure natural cp invariance of strong interactions? *Nuclear Physics B*, 166(3):493 – 506, 1980.

[15] Joshua P. Ellis. Tikz-feynman: Feynman diagrams with tikz. *Computer Physics Communications*, 210:103 – 123, 2017.

[16] C. Patrignani and Particle Data Group. Review of particle physics. *Chinese Physics C*, 40(10):100001, 2016.

[17] J.V. Sloan, M. Hotz, C. Boutan, R. Bradley, G. Carosi, D. Carter, J. Clarke, N. Crisosto, E.J. Daw, J. Gleason, J. Hoskins, R. Khatiwada, D. Lyapustin, A. Malagon, S. O'Kelley, R.S. Ottens, L.J. Rosenberg, G. Rybka, I. Stern, N.S. Sullivan, D.B. Tanner, K. van Bibber, A. Wagner, and D. Will. Limits on axion–photon coupling or on local axion density: Dependence on models of the milky way's dark halo. *Physics of the Dark Universe*, 14:95 – 102, 2016.

[18] M. Arik, S. Aune, K. Barth, A. Belov, H. Bräuninger, J. Bremer, V. Burwitz, G. Cantatore, J. M. Carmona, S. A. Cetin, J. I. Collar, E. Da Riva, T. Dafni, M. Davenport, A. Dermenev, C. Eleftheriadis, N. Elias, G. Fanourakis, E. Ferrer-Ribas, J. Galán, J. A. García, A. Gardikiotis, J. G. Garza, E. N. Gazis, T. Geralis, E. Georgiopoulou, I. Giomataris, S. Gninenko, M. Gómez Marzoa, M. D. Hasinoff, D. H. H. Hoffmann, F. J. Iguaz, I. G. Irastorza, J. Jacoby, K. Jakovčić, M. Karuza, M. Kavuk, M. Krčmar, M. Kuster, B. Lakić, J. M. Laurent, A. Liolios, A. Ljubičić, G. Luzón, S. Neff, T. Niinikoski, A. Nordt, I. Ortega, T. Papaevangelou, M. J. Pivovaroff, G. Raffelt, A. Rodríguez, M. Rosu, J. Ruz, I. Savvidis, I. Shilon, S. K. Solanki, L. Stewart, A. Tomás, T. Vafeiadis, J. Villar, J. K. Vogel, S. C. Yildiz, and K. Zioutas.

New solar axion search using the cern axion solar telescope with ^{4}He filling. *Phys. Rev. D*, 92:021101, Jul 2015.

[19] Dmitry Budker, Peter W. Graham, Micah Ledbetter, Surjeet Rajendran, and Alexander O. Sushkov. Proposal for a cosmic axion spin precession experiment (casper). *Phys. Rev. X*, 4:021030, May 2014.

[20] E Armengaud, F T Avignone, M Betz, P Brax, P Brun, G Cantatore, J M Carmona, G P Carosi, F Caspers, S Caspi, S A Cetin, D Chelouche, F E Christensen, A Dael, T Dafni, M Davenport, A V Derbin, K Desch, A Diago, B Döbrich, I Dratchnev, A Dudarev, C Eleftheriadis, G Fanourakis, E Ferrer-Ribas, J Galán, J A García, J G Garza, T Geralis, B Gimeno, I Giomataris, S Gninenko, H Gómez, D González-Díaz, E Guendelman, C J Hailey, T Hiramatsu, D H H Hoffmann, D Horns, F J Iguaz, I G Irastorza, J Isern, K Imai, A C Jakobsen, J Jaeckel, K Jakovčić, J Kaminski, M Kawasaki, M Karuza, M Krčmar, K Kousouris, C Krieger, B Lakić, O Limousin, A Lindner, A Liolios, G Luzón, S Matsuki, V N Muratova, C Nones, I Ortega, T Papaevangelou, M J Pivovaroff, G Raffelt, J Redondo, A Ringwald, S Russenschuck, J Ruz, K Saikawa, I Savvidis, T Sekiguchi, Y K Semertzidis, I Shilon, P Sikivie, H Silva, H ten Kate, A Tomas, S Troitsky, T Vafeiadis, K van Bibber, P Vedrine, J A Villar, J K Vogel, L Walckiers, A Weltman, W Wester, S C Yildiz, and K Zioutas. Conceptual design of the international axion observatory (iaxo). *Journal of Instrumentation*, 9(05):T05002, 2014.

[21] P. Sikivie. Experimental tests of the "invisible" axion. *Phys. Rev. Lett.*, 51:1415–1417, Oct 1983.

[22] P. Sikivie. Experimental tests of the "invisible" axion. *Phys. Rev. Lett.*, 52:695–695, Feb 1984.

[23] B. M. Brubaker et al. First results from a microwave cavity axion search at 24 micro-eV. 2016.

[24] Y. Inoue, Y. Akimoto, R. Ohta, T. Mizumoto, A. Yamamoto, and M. Minowa. Search for solar axions with mass around 1 ev using coherent conversion of axions into photons. *Physics Letters B*, 668(2):93 – 97, 2008.

[25] Klaus Ehret, Maik Frede, Samvel Ghazaryan, Matthias Hildebrandt, Ernst-Axel Knabbe, Dietmar Kracht, Axel Lindner, Jenny List, Tobias Meier, Niels Meyer, Dieter Notz, Javier Redondo, Andreas Ringwald, Günter Wiedemann, and Benno Willke. New {ALPS} results on hidden-sector lightweights. *Physics Letters B*, 689(4–5):149 – 155, 2010.

[26] M. Betz, F. Caspers, M. Gasior, M. Thumm, and S. W. Rieger. First results of the cern resonant weakly interacting sub-ev particle search (crows). *Phys. Rev. D*, 88:075014, Oct 2013.

[27] R. Ballou, G. Deferne, M. Finger, M. Finger, L. Flekova, J. Hosek, S. Kunc, K. Macuchova, K. A. Meissner, P. Pugnat, M. Schott, A. Siemko, M. Slunecka, M. Sulc, C. Weinsheimer, and J. Zicha. New exclusion limits on scalar and pseudoscalar axionlike particles from light shining through a wall. *Phys. Rev. D*, 92:092002, Nov 2015.

[28] L.M. Capparelli, G. Cavoto, J. Ferretti, F. Giazotto, A.D. Polosa, and P. Spagnolo. Axion-like particle searches with sub-thz photons. *Physics of the Dark Universe*, 12:37 – 44, 2016.

[29] T. Inada et al. Search for Two-Photon Interaction with Axionlike Particles Using High-Repetition Pulsed Magnets and Synchrotron X Rays. 2016.

[30] I. Ogawa, S. Matsuki, and K. Yamamoto. Interactions of cosmic axions with rydberg atoms in resonant cavities via the primakoff process. *Phys. Rev. D*, 53:R1740–R1744, Feb 1996.

[31] P. Sikivie, N. Sullivan, and D. B. Tanner. Proposal for axion dark matter detection using an *lc* circuit. *Phys. Rev. Lett.*, 112:131301, Mar 2014.

[32] P. Sikivie. Axion dark matter detection using atomic transitions. *Phys. Rev. Lett.*, 113:201301, Nov 2014.

[33] The MADMAX Working Group, Allen Caldwell, Gia Dvali, Bela Majorovits, Alexander Millar, Georg Raffelt, Javier Redondo, Olaf Reimann, Frank Simon, and Frank Steffen. Dielectric Haloscopes: A New Way to Detect Axion Dark Matter. 2016.

[34] SungWoo Youn. Axion research at capp/ibs. *International Journal of Modern Physics: Conference Series*, 43:1660193, 2016.

[35] B. R. Ko. Axion Haloscopes with Toroidal Geometry at CAPP/IBS. In *12th Patras Workshop on Axions, WIMPs and WISPs (AXION-WIMP 2016) Jeju Island, South Korea, June 20-24, 2016*, 2016.

[36] A. Derevianko, V. A. Dzuba, V. V. Flambaum, and M. Pospelov. Axio-electric effect. *Phys. Rev. D*, 82:065006, Sep 2010.

[37] K. Abe, K. Hieda, K. Hiraide, S. Hirano, Y. Kishimoto, K. Kobayashi, S. Moriyama, K. Nakagawa, M. Nakahata, H. Ogawa, N. Oka, H. Sekiya,

A. Shinozaki, Y. Suzuki, A. Takeda, O. Takachio, K. Ueshima, D. Umemoto, M. Yamashita, B.S. Yang, S. Tasaka, J. Liu, K. Martens, K. Hosokawa, K. Miuchi, A. Murata, Y. Onishi, K. Otsuka, Y. Takeuchi, Y.H. Kim, K.B. Lee, M.K. Lee, J.S. Lee, Y. Fukuda, Y. Itow, K. Masuda, Y. Nishitani, H. Takiya, H. Uchida, N.Y. Kim, Y.D. Kim, F. Kusaba, D. Motoki, K. Nishijima, K. Fujii, I. Murayama, and S. Nakamura. Search for solar axions in xmass, a large liquid-xenon detector. *Physics Letters B*, 724(1–3):46 – 50, 2013.

[38] A. V. Derbin, I. S. Drachnev, A. S. Kayunov, and V. N. Muratova. Constraints on the axion-electron coupling constant for solar axions appearing owing to bremsstrahlung and the compton process. *JETP Letters*, 95(7):339–344, 2012.

[39] E. Armengaud, Q. Arnaud, C. Augier, A. Benoit, A. Benoit, L. Bergé, T. Bergmann, J. Blümer, A. Broniatowski, V. Brudanin, P. Camus, A. Cazes, B. Censier, M. Chapellier, F. Charlieux, F. Couëdo, P. Coulter, G.A. Cox, T. de Boissière, M. De Jesus, Y. Dolgorouky, A.A. Drillien, L. Dumoulin, K. Eitel, D. Filosofov, N. Fourches, J. Gascon, G. Gerbier, M. Gros, L. Hehn, S. Henry, S. Hervé, G. Heuermann, N. Holtzer, V. Humbert, A. Juillard, C. Kéfélian, M. Kleifges, H. Kluck, V. Kozlov, H. Kraus, V.A. Kudryavtsev, H. Le Sueur, M. Mancuso, C. Marrache-Kikuchi, S. Marnieros, A. Menshikov, X-F. Navick, C. Nones, E. Olivieri, P. Pari, B. Paul, M.C. Piro, O. Rigaut, M. Robinson, S. Rozov, V. Sanglard, B. Schmidt, B. Siebenborn, D. Tcherniakhovski, M. Tenconi, L. Vagneron, R.J. Walker, M. Weber, E. Yakushev, and X. Zhang. Axion searches with the edelweiss-ii experiment. *Journal of Cosmology and Astroparticle Physics*, 2013(11):067, 2013.

[40] E. Aprile, F. Agostini, M. Alfonsi, K. Arisaka, F. Arneodo, M. Auger, C. Balan, P. Barrow, L. Baudis, B. Bauermeister, A. Behrens, P. Beltrame, K. Bokeloh, A. Brown, E. Brown, S. Bruenner, G. Bruno, R. Budnik, J. M. R. Cardoso, A. P. Colijn, H. Contreras, J. P. Cussonneau, M. P. Decowski, E. Duchovni, S. Fattori, A. D. Ferella, W. Fulgione, F. Gao, M. Garbini, C. Geis, L. W. Goetzke, C. Grignon, E. Gross, W. Hampel, R. Itay, F. Kaether, G. Kessler, A. Kish, H. Landsman, R. F. Lang, M. Le Calloch, D. Lellouch, C. Levy, S. Lindemann, M. Lindner, J. A. M. Lopes, K. Lung, A. Lyashenko, S. MacMullin, T. Marrodán Undagoitia, J. Masbou, F. V. Massoli, D. Mayani Paras, A. J. Melgarejo Fernandez, Y. Meng, M. Messina, B. Miguez, A. Molinario, M. Murra, J. Naganoma, K. Ni, U. Oberlack, S. E. A. Orrigo, E. Pantic, R. Persiani, F. Piastra, J. Pienaar, G. Plante, N. Priel, S. Reichard, C. Reuter, A. Rizzo, S. Rosendahl, J. M. F. dos Santos, G. Sartorelli, S. Schindler, J. Schreiner, M. Schumann, L. Scotto Lavina, M. Selvi, P. Shagin, H. Simgen, A. Teymourian, D. Thers, A. Tiseni, G. Trinchero, O. Vitells, H. Wang, M. Weber, and C. Weinheimer.

First axion results from the xenon100 experiment. *Phys. Rev. D*, 90:062009, Sep 2014.

[41] Y. S. Yoon, H. K. Park, H. Bhang, J. H. Choi, S. Choi, I. S. Hahn, E. J. Jeon, H. W. Joo, W. G. Kang, B. H. Kim, G. B. Kim, H. J. Kim, K. W. Kim, S. C. Kim, S. K. Kim, Y. D. Kim, Y. H. Kim, H. S. Lee, J. H. Lee, J. K. Lee, D. S. Leonard, J. Li, S. S. Myung, S. L. Olsen, and J. H. So. Search for solar axions with csi(tl) crystal detectors. *Journal of High Energy Physics*, 2016(6):11, 2016.

[42] Shigetaka Moriyama. Proposal to search for a monochromatic component of solar axions using ^{57}fe. *Phys. Rev. Lett.*, 75:3222–3225, Oct 1995.

[43] Yu. M. Gavrilyuk, A. N. Gangapshev, A. V. Derbin, I. S. Drachnev, V. V. Kazalov, V. V. Kobychev, V. V. Kuz'minov, V. N. Muratova, S. I. Panasenko, S. S. Ratkevich, D. A. Semenov, D. A. Tekueva, E. V. Unzhakov, and S. P. Yakimenko. New experiment on search for the resonance absorption of solar axion emitted in the m1 transition of 83kr nuclei. *JETP Letters*, 101(10):664–669, May 2015.

[44] T. Kaluza. Zum Unitätsproblem der Physik. *Sitzungsberichte der Königlich Preußischen Akademie der Wissenschaften (Berlin), Seite p. 966-972*, pages 966–972, 1921.

[45] Oskar Klein. Quantentheorie und f´ unfdimensionale relativit´ atstheorie. *Zeitschrift für Physik*, 37(12):895–906, 1926.

[46] Ignatios Antoniadis, Nima Arkani-Hamed, Savas Dimopoulos, and Gia Dvali. New dimensions at a millimeter to a fermi and superstrings at a tev. *Physics Letters B*, 436(3–4):257 – 263, 1998.

[47] Nima Arkani-Hamed, Savas Dimopoulos, and Gia Dvali. The hierarchy problem and new dimensions at a millimeter. *Physics Letters B*, 429(3–4):263 – 272, 1998.

[48] Nima Arkani-Hamed, Savas Dimopoulos, and Gia Dvali. Phenomenology, astrophysics, and cosmology of theories with submillimeter dimensions and tev scale quantum gravity. *Phys. Rev. D*, 59:086004, Mar 1999.

[49] Lawrence J. Hall and David Smith. Cosmological constraints on theories with large extra dimensions. *Phys. Rev. D*, 60:085008, Sep 1999.

[50] Jiro Murata and Saki Tanaka. A review of short-range gravity experiments in the lhc era. *Classical and Quantum Gravity*, 32(3):033001, 2015.

[51] D. J. Kapner, T. S. Cook, E. G. Adelberger, J. H. Gundlach, B. R. Heckel, C. D. Hoyle, and H. E. Swanson. Tests of the gravitational inverse-square law below the dark-energy length scale. *Phys. Rev. Lett.*, 98:021101, Jan 2007.

[52] Sanghyeon Chang, Shiro Tazawa, and Masahiro Yamaguchi. Axion model in extra dimensions with tev scale gravity. *Phys. Rev. D*, 61:084005, Mar 2000.

[53] Keith R. Dienes, Emilian Dudas, and Tony Gherghetta. Invisible axions and large-radius compactifications. *Phys. Rev. D*, 62:105023, Oct 2000.

[54] L. Di Lella, A. Pilaftsis, G. Raffelt, and K. Zioutas. Search for solar kaluza-klein axions in theories of low-scale quantum gravity. *Phys. Rev. D*, 62:125011, Nov 2000.

[55] Ernest Ma, Martti Raidal, and Utpal Sarkar. Low-scale axion from large extra dimensions. *Physics Letters B*, 504(4):296 – 300, 2001.

[56] Lisa Randall and Raman Sundrum. Large mass hierarchy from a small extra dimension. *Phys. Rev. Lett.*, 83:3370–3373, Oct 1999.

[57] Thomas Appelquist, Hsin-Chia Cheng, and Bogdan A. Dobrescu. Bounds on universal extra dimensions. *Phys. Rev. D*, 64:035002, Jun 2001.

[58] Hsin-Chia Cheng, Konstantin T. Matchev, and Martin Schmaltz. Radiative corrections to kaluza-klein masses. *Phys. Rev. D*, 66:036005, Aug 2002.

[59] Géraldine Servant and Tim M.P. Tait. Is the lightest kaluza–klein particle a viable dark matter candidate? *Nuclear Physics B*, 650(1–2):391 – 419, 2003.

[60] `https://www.nasa.gov/mission_pages/sunearth/science/solar-anatomy.html`.

[61] John T. Mariska. The quiet solar transition region. *Annual Review of Astronomy and Astrophysics*, 24(1):23–48, 1986.

[62] E. N. Parker. Nanoflares and the solar X-ray corona. *ApJ*, 330:474–479, July 1988.

[63] Yukio Katsukawa and Saku Tsuneta. Small fluctuation of coronal x-ray intensity and a signature of nanoflares. *ApJ*, 557(1):343, 2001.

[64] Yukio Katsukawa. Spatial and temporal extent of solar nanoflares and their energy range. *Publications of the Astronomical Society of Japan*, 55(5):1025–1031, 2003.

[65] R. Ramesh, K. Sasikumar Raja, C. Kathiravan, and A. Satya Narayanan. Low-frequency radio observations of picoflare category energy releases in the solar atmosphere. *The Astrophysical Journal*, 762(2):89, 2013.

[66] I. G. Hannah, H. S. Hudson, M. Battaglia, S. Christe, J. Kašparová, S. Krucker, M. R. Kundu, and A. Veronig. Microflares and the statistics of x-ray flares. *Space Science Reviews*, 159(1):263, 2011.

[67] Hannes Alfvén and B. Lindblad. Granulation, magneto-hydrodynamic waves, and the heating of the solar corona. *Monthly Notices of the Royal Astronomical Society*, 107(2):211–219, 1947.

[68] T. J. Okamoto, S. Tsuneta, T. E. Berger, K. Ichimoto, Y. Katsukawa, B. W. Lites, S. Nagata, K. Shibata, T. Shimizu, R. A. Shine, Y. Suematsu, T. D. Tarbell, and A. M. Title. Coronal transverse magnetohydrodynamic waves in a solar prominence. *Science*, 318(5856):1577–1580, 2007.

[69] Takenori J. Okamoto, Patrick Antolin, Bart De Pontieu, Han Uitenbroek, Tom Van Doorsselaere, and Takaaki Yokoyama. Resonant absorption of transverse oscillations and associated heating in a solar prominence. i. observational aspects. *The Astrophysical Journal*, 809(1):71, 2015.

[70] P. Antolin, T. J. Okamoto, B. De Pontieu, H. Uitenbroek, T. Van Doorsselaere, and T. Yokoyama. Resonant absorption of transverse oscillations and associated heating in a solar prominence. ii. numerical aspects. *The Astrophysical Journal*, 809(1):72, 2015.

[71] `http://hinode.nao.ac.jp/en/news/results/` `formation-mechanisms-of-the-solar-chromosphere-revealed-by-hinode-and-iris/`.

[72] L DiLella and K Zioutas. Observational evidence for gravitationally trapped massive axion(-like) particles. *Astroparticle Physics*, 19(1):145 – 170, 2003.

[73] K. Zioutas, K. Dennerl, L. DiLella, D. H. H. Hoffmann, J. Jacoby, and Th. Papaevangelou. Quiet-sun x-rays as signature for new particles. *The Astrophysical Journal*, 607(1):575, 2004.

[74] B. Morgan, N. J. C. Spooner, M. S. Armel-Funkhouser, D. P. Snowden-Ifft, D. H. H. Hoffmann, K. Zioutas, and J. Jacoby. Searches for solar Kaluza–Klein axions with gas TPCs. *Astropart. Phys.*, 23:287–302, 2005.

[75] D. Naples, R. Ayad, G. Bonvincini, M. Katz-Hyman, J. Martoff, J. Miyamoto, V. Paolone, V. Savinov, and I. Shipsey. Search for axion-like particles from the sun in an underground negative-ion tpc. *Nuclear Physics B - Proceedings Supplements*, 134:130 – 132, 2004.

[76] Javier Galan, Gilles Gerbier, Ioannis Giomataris, Thomas Papaevangelou, and Ilias Savvidis. Extending axions searches with a spherical TPC. 2013.

[77] R. Horvat, M. Krčmar, and B. Lakić. Recent searches for solar axions and large extra dimensions. *Phys. Rev. D*, 65:087701, Mar 2002.

[78] R. Horvat, M. Krčmar, and B. Lakić. Cern axion solar telescope as a probe of large extra dimensions. *Phys. Rev. D*, 69:125011, Jun 2004.

[79] K. Abe, K. Hieda, K. Hiraide, S. Hirano, Y. Kishimoto, K. Kobayashi, S. Moriyama, K. Nakagawa, M. Nakahata, H. Nishiie, H. Ogawa, N. Oka, H. Sekiya, A. Shinozaki, Y. Suzuki, A. Takeda, O. Takachio, K. Ueshima, D. Umemoto, M. Yamashita, B.S. Yang, S. Tasaka, J. Liu, K. Martens, K. Hosokawa, K. Miuchi, A. Murata, Y. Onishi, Y. Otsuka, Y. Takeuchi, Y.H. Kim, K.B. Lee, M.K. Lee, J.S. Lee, Y. Fukuda, Y. Itow, Y. Nishitani, K. Masuda, H. Takiya, H. Uchida, N.Y. Kim, Y.D. Kim, F. Kusaba, D. Motoki, K. Nishijima, K. Fujii, I. Murayama, and S. Nakamura. Xmass detector. *Nuclear Instruments and Methods in Physics Research Section A: Accelerators, Spectrometers, Detectors and Associated Equipment*, 716:78 – 85, 2013.

[80] Y. Suzuki. Low-energy solar neutrino detection by using liquid xenon. In *Workshop on Solar Neutrinos below 1-MeV: NuLow Sudbury, Canada, June 15, 2000*, 2000.

[81] Katsuki Hiraide. The data acquisition system of the xmass experiment. *Journal of Physics: Conference Series*, 664(8):082018, 2015.

[82] N.Y. Kim, K. Abe, K. Hieda, K. Hiraide, S. Hirano, Y. Kishimoto, K. Kobayashi, S. Moriyama, K. Nakagawa, M. Nakahata, H. Nishiie, H. Ogawa, N. Oka, H. Sekiya, A. Shinozaki, Y. Suzuki, A. Takeda, O. Takachio, K. Ueshima, D. Umemoto, M. Yamashita, B.S. Yang, S. Tasaka, J. Liu, K. Martens, K. Hosokawa, K. Miuchi, A. Murata, Y. Onishi, Y. Otsuka, Y. Takeuchi, Y.H. Kim, K.B. Lee, M.K. Lee, J.S. Lee, Y. Fukuda, Y. Itow, Y. Nishitani, K. Masuda, H. Takiya, H. Uchida, Y.D. Kim, F. Kusaba, D. Motoki, K. Nishijima, K. Fujii, I. Murayama, and S. Nakamura. Micro-source development for {XMASS} experiment. *Nuclear Instruments and Methods in Physics Research Section A: Accelerators, Spectrometers, Detectors and Associated Equipment*, 784:499 – 503, 2015. Symposium on Radiation Measurements and Applications 2014 (SORMA XV).

[83] T. Doke, R. Sawada, and H. Tawara. Non-proportionality of the scintillation yield in liquid xenon and its effect on the energy resolution for gamma-rays.

In *Technique and application of xenon detectors. Proceedings, International Workshop, Kashiwa, Japan, December 3-4, 2001*, pages 17–27, 2001.

[84] S. Agostinelli, J. Allison, K. Amako, J. Apostolakis, H. Araujo, P. Arce, M. Asai, D. Axen, S. Banerjee, G. Barrand, F. Behner, L. Bellagamba, J. Boudreau, L. Broglia, A. Brunengo, H. Burkhardt, S. Chauvie, J. Chuma, R. Chytracek, G. Cooperman, G. Cosmo, P. Degtyarenko, A. Dell'Acqua, G. Depaola, D. Dietrich, R. Enami, A. Feliciello, C. Ferguson, H. Fesefeldt, G. Folger, F. Foppiano, A. Forti, S. Garelli, S. Giani, R. Giannitrapani, D. Gibin, J.J. Gómez Cadenas, I. González, G. Gracia Abril, G. Greeniaus, W. Greiner, V. Grichine, A. Grossheim, S. Guatelli, P. Gumplinger, R. Hamatsu, K. Hashimoto, H. Hasui, A. Heikkinen, A. Howard, V. Ivanchenko, A. Johnson, F.W. Jones, J. Kallenbach, N. Kanaya, M. Kawabata, Y. Kawabata, M. Kawaguti, S. Kelner, P. Kent, A. Kimura, T. Kodama, R. Kokoulin, M. Kossov, H. Kurashige, E. Lamanna, T. Lampén, V. Lara, V. Lefebure, F. Lei, M. Liendl, W. Lockman, F. Longo, S. Magni, M. Maire, E. Medernach, K. Minamimoto, P. Mora de Freitas, Y. Morita, K. Murakami, M. Nagamatu, R. Nartallo, P. Nieminen, T. Nishimura, K. Ohtsubo, M. Okamura, S. O'Neale, Y. Oohata, K. Paech, J. Perl, A. Pfeiffer, M.G. Pia, F. Ranjard, A. Rybin, S. Sadilov, E. Di Salvo, G. Santin, T. Sasaki, N. Savvas, Y. Sawada, S. Scherer, S. Sei, V. Sirotenko, D. Smith, N. Starkov, H. Stoecker, J. Sulkimo, M. Takahata, S. Tanaka, E. Tcherniaev, E. Safai Tehrani, M. Tropeano, P. Truscott, H. Uno, L. Urban, P. Urban, M. Verderi, A. Walkden, W. Wander, H. Weber, J.P. Wellisch, T. Wenaus, D.C. Williams, D. Wright, T. Yamada, H. Yoshida, and D. Zschiesche. Geant4—a simulation toolkit. *Nuclear Instruments and Methods in Physics Research Section A: Accelerators, Spectrometers, Detectors and Associated Equipment*, 506(3):250 – 303, 2003.

[85] Kazuyoshi Kobayashi. Surface purity control during xmass detector refurbishment. *AIP Conference Proceedings*, 1672(1):050003, 2015.

[86] G. L. Fogli, E. Lisi, A. Marrone, D. Montanino, and A. Palazzo. Getting the most from the statistical analysis of solar neutrino oscillations. *Phys. Rev. D*, 66:053010, Sep 2002. Pull term.

[87] K. Abe et al. Direct dark matter search by annual modulation in XMASS-I. *Phys. Lett.*, B759:272–276, 2016.

[88] Adrian Ayala, Inma Domínguez, Maurizio Giannotti, Alessandro Mirizzi, and Oscar Straniero. Revisiting the bound on axion-photon coupling from globular clusters. *Phys. Rev. Lett.*, 113:191302, Nov 2014.

[89] N. Vinyoles, A. Serenelli, F.L. Villante, S. Basu, J. Redondo, and J. Isern. New axion and hidden photon constraints from a solar data global fit. *Journal of Cosmology and Astroparticle Physics*, 2015(10):015, 2015.

[90] Olivier Wantz and E. P. S. Shellard. Axion cosmology revisited. *Phys. Rev. D*, 82:123508, Dec 2010.